

# Phase-field crystal study of grain-boundary premelting

Jesper Mellenthin,<sup>1,2</sup> Alain Karma,<sup>3</sup> and Mathis Plapp<sup>1</sup>

<sup>1</sup>*Physique de la Matière Condensée, Ecole Polytechnique, CNRS, 91128 Palaiseau, France*

<sup>2</sup>*Department of Physics, Northeastern University, Boston, Massachusetts 02115*

<sup>3</sup>*Physics Department, Northeastern University, Boston, Massachusetts 02115*

(Dated: November 20, 2008)

We study the phenomenon of grain-boundary premelting for temperatures below the melting point in the phase-field crystal model of a pure material with hexagonal ordering in two dimensions. We investigate the structures of symmetric tilt boundaries as a function of misorientation  $\theta$  for two different inclinations and compute in the grand canonical ensemble the “disjoining potential”  $V(w)$  that describes the fundamental interaction between crystal-melt interfaces as a function of the premelted layer width  $w$ , which is defined here in terms of the excess mass of the grain boundary via a Gibbs construction. The results reveal qualitatively different behaviors for high-angle grain boundaries that are uniformly wetted, with  $w$  diverging logarithmically as the melting point is approached from below, and low-angle boundaries that are punctuated by liquid pools surrounding dislocations, separated by solid bridges. The latter persist over a superheated range of temperature. This qualitative difference between high- and low-angle boundaries is reflected in the  $w$ -dependence of the disjoining potential that is purely repulsive ( $V'(w) < 0$  for all  $w$ ) for misorientations larger than a critical angle  $\theta_c$ , but switches from repulsive at small  $w$  to attractive at large  $w$  for  $\theta < \theta_c$ . In the latter case,  $V(w)$  has a minimum that corresponds to a premelted boundary of finite width at the melting point. Furthermore, we find that the standard wetting condition  $\gamma_{gb}(\theta_c) = 2\gamma_{sl}$  gives a much too low estimate of  $\theta_c$  when a low-temperature value of the grain boundary energy  $\gamma_{gb}$  is used. In contrast, a reasonable lower-bound estimate can be obtained if  $\gamma_{gb}$  is extrapolated to the melting point, taking into account both the elastic softening of the material at high homologous temperature and local melting around dislocations.

PACS numbers: 61.72.Mm, 64.70.D-, 81.16.Rf, 81.30.Fb

## I. INTRODUCTION AND SUMMARY

The presence of liquid films at grain boundaries for temperatures below the melting point can alter macroscopic properties of polycrystalline materials and dramatically reduce resistance to shear stresses. The latter can lead to catastrophic material failure as exemplified by hot cracking during high-temperature processing of metallic alloys<sup>1,2</sup>. While there is indirect experimental evidence for the occurrence of grain-boundary premelting in both pure materials<sup>3,4</sup> and alloys<sup>2,5</sup>, it is inherently difficult to image and to measure thermodynamic properties of nanometer-width liquid films. One exception is optical microscopy of colloidal crystals, which has produced striking “atomistic”-scale images of premelted grain boundaries<sup>6</sup>. Even in this case, however, the lack of precise control of grain geometry and external conditions makes it hard to determine the fundamental nature of the premelting transition.

Molecular dynamics (MD) simulations provide in principle a powerful alternative to experiment for studying grain-boundary premelting. MD studies using Lennard-Jones<sup>7,8,9</sup> and interatomic potentials for metals<sup>10,11,12</sup> and semiconductors such as silicon<sup>13</sup> have reported evidence for disordered layers at grain boundaries at different temperatures below<sup>7,8,9,10,11,13</sup> and above<sup>12</sup> the melting point. In addition, such layers have been reported to exhibit fluid-like properties in a MD study of grain-boundary shearing in a Lennard-Jones system where the shear modulus decreased sharply below the

melting point<sup>9</sup>. The large fluctuations inherent in MD simulations, however, make it generally hard to compute precisely the thermodynamic properties of grain boundaries at high homologous temperature and to quantify the interaction between crystal-melt interfaces.

A remarkable study of grain-boundary premelting was carried out by Kikuchi and Cahn<sup>14</sup> using a lattice gas model and a cluster variation approximation for the evaluation of its thermodynamic properties. Their results were later corroborated by Monte Carlo simulations of the same model<sup>15</sup>. They indeed found a liquid-like layer at the grain boundary for temperatures well below the melting point. The width of this layer diverges logarithmically when the melting point is approached. While this study gave valuable insights, it did not yield a complete picture of grain-boundary premelting since the construction of the lattice-gas model leads to numerous geometrical constraints, such that only a single misorientation could be investigated.

From a basic thermodynamic viewpoint, grain-boundary premelting is governed by the balance between bulk and interfacial free energies. While the difference in bulk free energies per unit volume between solid and liquid<sup>16</sup>,  $\Delta G(T) \equiv G_s(T) - G_l(T)$ , always favors a crystalline state below the melting point, the interfacial free energy favors the formation of a liquid layer for wetting conditions. The total excess free energy (per unit area of grain boundary) that reflects both contributions can be

written in the form<sup>17</sup>

$$G_{\text{exc}}(w, T) = \Delta G(T)w + 2\gamma_{sl} + V(w), \quad (1)$$

where  $w$  denotes the liquid layer width and the last two terms on the right-hand-side represent the interfacial free energy. The latter must reduce to twice the excess free energy of the solid-liquid interface,  $2\gamma_{sl}$ , when the two solid-liquid interfaces are well separated, but generally contains an additional contribution  $V(w)$  when their separation becomes comparable to the intrinsic nanometer-width  $\delta$  of an isolated solid-liquid interface. This additional contribution, referred to hereafter as the “disjoining potential,” represents the interaction due to the overlap of two solid-liquid interfaces, which drives the formation of a liquid layer under wetting conditions, or conversely joins two crystals for non-wetting conditions. Its derivative  $V'(w)$  is directly analogous to the disjoining pressure used in the physics of thin liquid films<sup>18</sup>.

In this paper, we study grain-boundary premelting using the phase-field crystal (PFC) modeling approach<sup>19,20,21,22,23,24</sup> inspired from classical density-functional theory<sup>25</sup>. In the present context, this mean-field approach has the advantage of resolving the atomic-scale density-wave structure of a polycrystalline material while, at the same time, averaging out fluctuations. Therefore, it is ideally suited for computing quantitatively the disjoining potential and for elucidating its relationship to atomic grain-boundary structure. In a recent study, Berry *et al.* observed melting at grain boundaries in three-dimensional phase-field crystal simulations for bcc ordering<sup>26</sup>, thereby suggesting the usefulness of this method for investigating fundamental aspects of this phenomenon. Thermodynamic properties of premelted grain boundaries, however, were not studied in detail in this work. The present work focuses on the quantitative study of premelting in the general framework of Eq. (1) with the appropriate choice of thermodynamic ensemble for the phase-field crystal model, for two-dimensional crystals with hexagonal symmetry. We compute explicitly the dependence of the disjoining potential on layer width and determine wetting conditions as a function of grain-boundary orientation. This allows us to make contact with sharp<sup>1,8</sup> and diffuse-interface<sup>1,27,28</sup> theories of interfacial premelting. Like MD studies with truncated short-range interatomic potentials<sup>7,8,9,10,11,12,13</sup>, these theories neglect the effects of long-range dispersion forces considered in statistical theories of grain-boundary melting<sup>29</sup> and in theoretical<sup>30</sup> and experimental<sup>31</sup> studies of intergranular phases in ceramic materials. These forces are also neglected in the present phase-field crystal study that focuses on the structural component of the disjoining potential due to partial crystal ordering within premelted layers.

## A. Sharp- and diffuse-interface theories

In the simplest theory, a “wet” grain boundary is modeled as a thin layer of liquid sandwiched between two solid-liquid boundaries, assumed to be sharp and straight. If only short-range forces are present, an exponential interaction between the interfaces is expected for large film thickness<sup>14</sup>. This suggests to write<sup>1,8</sup>

$$V(w) = \Delta\gamma \exp\left(-\frac{w}{\delta}\right), \quad (2)$$

where the prefactor  $\Delta\gamma \equiv \gamma_{gb}^0 - 2\gamma_{sl}$  guarantees that the total interfacial free energy  $V(w) + 2\gamma_{sl}$  in Eq. (1) reduces to the energy  $\gamma_{gb}^0$  of a “dry” grain boundary in the limit of vanishing liquid layer width. Minimization of the total excess free energy in Eq. (1) with respect to  $w$ , with  $V(w)$  defined by Eq. (2), predicts that, for  $\Delta\gamma > 0$ , the liquid layer width vanishes for temperatures less than a “bridging temperature”  $T_b$ , defined by  $\Delta G(T_b) = -\Delta\gamma/\delta$ , and increases smoothly as

$$w(T) = -\delta \ln(-\Delta G(T)\delta/\Delta\gamma) \text{ for } T_b < T < T_m, \quad (3)$$

ultimately diverging as the melting temperature  $T_m$  is approached from below. For  $\Delta\gamma < 0$ , in contrast, boundaries remain completely dry ( $w(T) = 0$ ) for all  $T$  up to a maximum temperature  $T^*$  defined by

$$\Delta G(T^*) = -\Delta\gamma/\delta, \quad (4)$$

and are in metastable equilibrium with respect to the liquid in the superheated range  $T_m < T < T^*$ .

The grain-boundary energy is generally defined as the total excess free energy of the boundary with respect to the solid, or  $\gamma_{gb}(T) = G_{\text{exc}}(w(T), T)$  here. Therefore, in the wetting case ( $\Delta\gamma > 0$ ), this energy is constant and simply equal to  $\gamma_{gb}^0$  for  $T < T_b$ , consistent with the requirement that  $\gamma_{gb}(0) = \gamma_{gb}^0$ , but decreases for  $T > T_b$  until reaching  $2\gamma_{sl}$  at the melting point where  $w$  diverges. Substituting Eq. (3) into Eq. (1) gives

$$\gamma_{gb}(T) - 2\gamma_{sl} = -\delta \Delta G(T) [1 + \ln(-\Delta G(T)\delta/\Delta\gamma)], \quad (5)$$

for  $T_b < T < T_m$ , which has limits  $\Delta\gamma$  and zero at  $T = T_b$  and  $T = T_m$ , respectively. In contrast, for non-wetting conditions ( $\Delta\gamma < 0$ ), this theory predicts that the grain-boundary energy retains its dry value for all temperatures:  $\gamma_{gb}(T) = \gamma_{gb}^0$  for  $T < T^*$ .

Phase-field theories of interfacial premelting<sup>27,28</sup> where solid-liquid interfaces are inherently spatially diffuse have yielded predictions that are in part consistent with the above picture, but also point to the possibility of more complex premelting behaviors. The most detailed studies have been carried out in models where the crystal orientation is represented by a scalar field coupled to the standard scalar phase field that measures the local crystal disorder. For wetting conditions, those models predict either a smooth increase of  $w$  with temperature below  $T_m$ , qualitatively similar to the behavior predicted by Eq. (3),

or the existence of first-order transitions between grain-boundary states of different widths<sup>27,28</sup>, in analogy with the theory of critical-point wetting<sup>32</sup>. These predictions, however, depend generally on the choice of phenomenological thermodynamic functions and parameters in those models that cannot be derived directly from microscopic physics, and thus are hard to relate to real systems. The phase-field crystal model, in contrast, has the advantage of removing much of the arbitrariness inherent in conventional phase-field theories. It explicitly describes the dislocation structure of grain boundaries and is formulated in terms of physical quantities, such as the liquid structure factor, that can be either measured experimentally or computed using MD simulations. Hence, this model can in principle make quantitative predictions that can be compared to both experiments or MD simulations as demonstrated recently for isolated solid-liquid interfaces in a bcc system<sup>33,34</sup>.

### B. Disjoining potential and layer width definitions in the phase-field crystal model

Before summarizing our main results, some thermodynamic considerations relevant for the present phase-field crystal study are worthy of brief mention. First, while premelting for pure materials has traditionally been discussed in the Gibbs ensemble of Eq. (1) with constant  $T$ , pressure  $p$ , and particle number  $N$ , the choice of the grand canonical ensemble with constant  $T$ , chemical potential  $\mu$ , and volume  $V$ , is more suited for the PFC model where the Helmholtz free energy is a function of the density and simulations are carried out at fixed  $V$ . Thus, the disjoining potential is defined here in terms of the excess of the grand potential in complete analogy with Eq. (1), i.e. it represents the total interfacial contribution of this excess minus its asymptotic value for well-separated interfaces equal to  $2\gamma_{sl}$ . For reasons detailed below, it is simpler to study premelting as a function of  $\mu$  rather than  $T$  in the PFC model. Both are intensive variables, and the results are expected to be equivalent. In particular, the departure of the chemical potential from its equilibrium value  $\mu_{eq} - \mu$  in the grand canonical ensemble is analogous to the departure of the temperature from the melting point  $T - T_m$  in the Gibbs ensemble, with the solid (liquid) being stable for negative (positive) values of both quantities in their respective ensembles. For convenience, even though we work in the grand canonical ensemble with  $\mu$  as control parameter, we often refer interchangeably hereafter to temperature and chemical potential to facilitate the comparison of our results to previous theories and experiments.

Second, we define the liquid layer width using a Gibbs construction. We first determine the excess mass carried by the grain boundary, which is simply the total mass of the bicrystal system with a grain boundary at fixed  $\mu$  minus the mass of a single crystal occupying the same volume at the same  $\mu$ . The film thickness  $w$  is then

defined by equating this excess mass to the product of  $w$  and the difference between solid and liquid densities. The advantage of this thermodynamic approach is that it gives a precise definition of  $w$  that remains applicable even when the liquid layer is not spatially uniform along the grain boundary, as is the case here for small misorientations. This definition of course reduces to the standard definition of the layer width in the limit where the liquid layer width is much larger than the intrinsic solid-liquid interface width ( $w \gg \delta$ ).

### C. Main results

Let us now summarize our main results as they relate to the theories reviewed above. The structure and properties of symmetric tilt boundaries were studied as a function of misorientation  $\theta$  for two different inclinations where the symmetry axis (from which each crystal is rotated by  $\pm\theta/2$ ) is parallel ( $\phi = 0$ ) or at a  $30^\circ$  angle ( $\phi = 30^\circ$ ) to any of the six equivalent close-packed directions of the hexagonal crystal.

We find that high-angle boundaries behave essentially as predicted by the sharp-interface theory. They are dry well below the melting point and become uniformly wetted with a liquid layer of roughly constant width along the boundary. The latter diverges logarithmically as the melting point is approached from below, consistent with a disjoining potential that is reasonably well approximated by the simple exponential form of Eq. (2). In contrast, the behavior of low-angle boundaries in the PFC model is not correctly predicted by the sharp-interface theory, both qualitatively and quantitatively. The main qualitative difference is that grain boundaries in the PFC model do not remain dry with zero width as predicted by this theory. They exhibit local melting around dislocations, as previously seen in Ref.<sup>26</sup>, and the resulting liquid pools cause  $w$  to increase smoothly with temperature (i.e.,  $\mu_{eq} - \mu$  in the grand canonical phase-field crystal simulations), although  $w$  remains finite at the melting point and into the superheated range ( $\mu_{eq} - \mu > 0$ ) where these boundaries are metastable. At a more quantitative level, dislocation-induced premelting contributes to the reduction in the grain-boundary energy from its low-temperature value, which can be larger than  $2\gamma_{sl}$  even for small misorientations, to a value less than  $2\gamma_{sl}$  near the melting point. The other factor contributing to this reduction is the elastic softening of the material at the melting point discussed below.

Dislocation-induced premelting of low-angle boundaries is reflected in the  $w$ -dependence of the disjoining potential  $V(w)$  that exhibits a minimum at a finite width  $w = w_m$ , which corresponds to the equilibrium layer width at the melting point. Therefore, this potential is repulsive for  $w < w_m$  and attractive for  $w > w_m$ . In contrast, it is predicted to be attractive for all  $w$  in the sharp-interface theory. The high- and low-angle regimes can be formally distinguished by defining a critical mis-

orientation  $\theta_c$  such that, for  $\theta > \theta_c$ , the disjoining potential is purely repulsive for all  $w$ , and, for  $\theta < \theta_c$ , exhibits a minimum with short-range repulsion and long-range attraction. Our results suggest that the transition between these two regimes is smooth, with the equilibrium layer width at the melting point diverging in the limit where  $\theta$  approaches  $\theta_c$  from below, although the nature of this divergence is hard to pinpoint precisely. It should be emphasized that the transition does not correspond to a sharp transition in the geometry of the grain boundary. Rather, the critical angle falls into a range where the geometry of the grain boundary is somewhere in between the two extremes described above. Namely, when the melting point is approached from below for  $\theta$  slightly above or below  $\theta_c$ , the grain boundary consists of liquid pools separated by “bridges”, but the distance between the dislocations is comparable to the pool diameter, so that the pools start to overlap and the material of the bridges is no longer fully solid.

While the main results described so far are ostensibly independent of inclination, we find some additional  $\phi$ -dependent features that require refinement of the above picture. For the  $\phi = 30^\circ$  inclination, which has the simplest behavior, the liquid pools were always found to be centered around isolated dislocations for low-angle boundaries, as seen qualitatively in Ref.<sup>26</sup>, and to merge progressively to form a uniform film with increasing misorientation. In contrast, for the  $\phi = 0$  inclination, which was investigated here in greater detail, discontinuous structural transitions were seen between different grain-boundary states. In one state, each dislocation is surrounded by its own liquid pool. In the other state, two dislocations combine to share a common liquid pool. The structural transition between these two states only occurs above a small misorientation well below  $\theta_c$ . The transition first occurs in the overheated states above the melting point, and shifts to lower values of  $\mu_{eq} - \mu$  with increasing misorientation. Furthermore, the transition is hysteretic, such that two grain-boundary states with different liquid-pool structures can coexist over a certain range of  $\mu$ . The jump in  $w$  at the transitions between different states, which measures effectively the change in liquid fraction associated with the pairing of liquid pools, is small. Hence, it cannot be ruled out that these transitions would be smeared by fluctuations and not directly observable as sharp transitions in a real system.

The most relevant aspect of our results for experiment is the quantitative prediction of the critical wetting angle  $\theta_c$  above which the liquid layer width diverges at the melting point. In the sharp-interface theory, this angle is predicted by the standard wetting condition  $\Delta\gamma(\theta) = \gamma_{gb}^0(\theta) - 2\gamma_{sl} = 0$ , where  $\gamma_{gb}^0(\theta)$  is taken to be the completely dry grain-boundary energy far below the melting point. As such, this condition predicts a value of  $\theta_c$  that is much smaller than observed in the phase-field crystal simulations. This failure is due to the fact that the sharp-interface theory predicts that the grain-boundary energy is constant for nonwetting condi-

tions. As noted earlier, this energy is reduced by both dislocation-induced premelting and the elastic softening of the material at high homologous temperature. Therefore, one would expect a better estimate of  $\theta_c$  to be obtained by comparing  $2\gamma_{sl}$  to a value of the grain-boundary energy at the melting point,  $\gamma_{gb}^m(\theta)$ , which is generally much lower than  $\gamma_{gb}^0(\theta)$  as found in a MD study of a tilt boundary in pure Cu<sup>35</sup>. Note that  $\gamma_{gb}^m(\theta) \rightarrow 2\gamma_{sl}$  when  $\theta$  approaches  $\theta_c$  from below, and  $\gamma_{gb}^m = 2\gamma_{sl}$  for all  $\theta$  larger than  $\theta_c$ .

Of course, the precise determination of  $\gamma_{gb}^m(\theta)$  generally requires a complete solution of the problem since it depends on the structural details of the premelted grain-boundary structure. A somewhat better prediction of  $\theta_c$  can nonetheless be obtained by an estimation of the grain-boundary energy at the melting point that takes into account the bulk elastic softening of the material and melting around dislocations. As in previous PFC studies<sup>19,20</sup>, we find that for low-angle grain boundaries  $\gamma_{gb}$  is well described by the Read-Shockley law<sup>36</sup>. The physical parameters entering this law are the shear modulus  $G$  and the dislocation core radius  $r_0$ . Hence we have, for small angles,  $\gamma_{gb} \approx \gamma_{RS}(\theta, G, r_0)$ . Elastic softening and dislocation premelting are reflected in the temperature dependence of these quantities. The shear modulus, which can be calculated analytically in the PFC model, has large variations: denoting by  $G_0$  and  $G_m$  its values at zero temperature and at the melting point, respectively, we find typically  $G_0/G_m \approx 3$ . The variation of the core radius is obtained by fitting our simulation data with the Read-Shockley law and describes phenomenologically the dislocation premelting. We observe an increase of the core radius at the melting point by about 40% with respect to its zero-temperature value.

It should be noted that, whereas data for the variation of the elastic constants are readily available, the variation of the core radius is a result of the premelting around dislocations and hence difficult to quantify in experiments or MD simulations. This suggests that it is useful to consider two successive approximations to improve the estimate of the critical wetting angle. If only the elastic softening is included, we can exploit the fact that in the Read-Shockley law the grain-boundary energy is simply proportional to the shear modulus. Therefore, we have  $\gamma_{gb}^m(\theta) \approx \gamma_{gb}^0(\theta)G_m/G_0$ , and thus the modified wetting condition  $\gamma_{gb}^0(\theta_c)G_m/G_0 \approx 2\gamma_{sl}$ . If, in addition, the variation of the core radius is included, the estimate for the grain-boundary energy becomes  $\gamma_{gb}^m(\theta) \approx \gamma_{gb}^0\gamma_{RS}(\theta, G_m, r_0(T_m))/\gamma_{RS}(\theta, G_0, r_0(0))$ , where  $r_0(0)$  and  $r_0(T_m)$  are the values of the core radius at zero temperature and the melting point, respectively. Inserting the explicit expression of the Read-Shockley law yields the improved wetting condition

$$\gamma_{gb}^m(\theta_c) \approx \gamma_{gb}^0(\theta_c) \frac{G_m}{G_0} \frac{1 - \ln[2\pi\theta_c r_0(T_m)/(\alpha a)]}{1 - \ln[2\pi\theta_c r_0(0)/(\alpha a)]} \approx 2\gamma_{sl}, \quad (6)$$

where  $a$  is the lattice constant of the hexagonal crys-

tal, and  $\alpha = \sqrt{3}/2$  is the distance between close-packed planes in the hexagonal structure, expressed in units of the lattice spacing. Concretely, for the  $\phi = 0$  inclination, the phase-field crystal simulations yield  $\theta_c \approx 14^\circ$ . The standard wetting condition  $\gamma_{gb}^0 = 2\gamma_{sl}$  predicts a completely erroneous value of  $\theta_c$  of about  $2^\circ$ . The condition including only the elastic softening predicts  $\theta_c \approx 6^\circ$ , whereas the condition of Eq. (6) including both effects yields  $\theta_c \approx 10^\circ$ . The remaining discrepancy with the value from simulations reflects the fact that the Read-Shockley law is no longer valid when liquid pools start to overlap and the structure of the grain boundary is no longer well described by an array of isolated dislocations, which is precisely the range where  $\theta \approx \theta_c$ . While, therefore, even the best estimate is still of limited accuracy, it sheds light on several physical effects determining the critical wetting angle that have not been previously appreciated.

Finally, the failure of the sharp-interface theory to predict the critical wetting angle obviously makes this theory inadequate in predicting the superheated range of temperature for low-angle boundaries. For  $\phi = 0$ , this theory predicts that only boundaries with  $\theta$  less than  $\theta_c \approx 2^\circ$  are superheated, while boundaries in the PFC model can be superheated for  $\theta$  up to  $\theta_c \approx 14^\circ$ , with this range vanishing as  $\theta \rightarrow \theta_c$ . If the computed values for the grain-boundary energy at the melting point are used instead of the low-temperature values, the sharp-interface prediction yields the right order of magnitude for the superheated range for angles close to  $\theta_c$ , but largely overestimates this range for low-angle grain boundaries.

The remainder of the paper is organized as follows. In Sec. II, we briefly review the phase-field crystal model and describe our numerical methods. In Sec. III, we outline the procedure for obtaining the liquid layer width, the grain-boundary energy, and the disjoining potential from our simulation data. Our results are presented in Sec. IV, and discussed in Sec. V. Finally, concluding remarks and future prospects are given in Sec. VI.

## II. PHASE-FIELD CRYSTAL MODEL

### A. Basic equations and properties

We consider the simplest PFC model defined by the dimensionless free energy functional<sup>19,20</sup>

$$\mathcal{F} = \int d\vec{r} \left\{ \frac{\psi}{2} [-\epsilon + (\nabla^2 + 1)^2] \psi + \frac{1}{4} \psi^4 \right\}. \quad (7)$$

which is a transposition to crystalline solids of the Swift-Hohenberg model of pattern formation<sup>37</sup>. Furthermore, we define the dimensionless chemical potential

$$\mu = \frac{\delta \mathcal{F}}{\delta \psi} = -\epsilon \psi + (\nabla^2 + 1)^2 \psi + \psi^3. \quad (8)$$

The dimensionless functional in Eq. (7) can be obtained by a suitable rescaling of a dimensional free-energy func-

tional which, in turn, can be related to classical density-functional theory. Since these transformations have been discussed in detail elsewhere<sup>19,20,24,33,34</sup>, they do not need to be repeated here.

The phase diagram of this model has also been discussed previously<sup>20</sup>. However, since a precise characterization of the bulk phases is important for the present work, we resume here the main steps that are necessary to obtain the properties which are needed in the subsequent developments. To construct the phase diagram, we calculate separately the free-energy density (free energy per unit surface in two dimensions) as a function of the mean density  $\bar{\psi}$  in the solid, denoted by  $f_s(\bar{\psi})$ , and in the liquid,  $f_l(\bar{\psi})$ , using Eq. (7). Since the density is uniform in the liquid,  $f_l(\bar{\psi})$  is obtained directly from Eq. (7),

$$f_l = -(\epsilon - 1) \frac{\bar{\psi}^2}{2} + \frac{\bar{\psi}^4}{4}. \quad (9)$$

It is possible to obtain an analytical expression for  $f_s$  in the one-mode approximation, in which only the contribution of the principal reciprocal-lattice vectors is taken into account. Then, the density for the two-dimensional hexagonal structure can be written<sup>20</sup> as

$$\psi_s(x, y) = \bar{\psi} + A_t \left[ \cos(qx) \cos\left(\frac{qy}{\sqrt{3}}\right) - \frac{1}{2} \cos\left(\frac{2qy}{\sqrt{3}}\right) \right]. \quad (10)$$

This solution ansatz is inserted into the free energy, Eq. (7). Integrating over a unit cell and minimizing the free energy with respect to  $A_t$  and  $q$  leads to

$$A_t = \frac{4}{5} \left( \bar{\psi} \pm \frac{1}{3} \sqrt{15\epsilon - 36\bar{\psi}^2} \right), \quad (11)$$

where the  $\pm$  signs are for positive and negative  $\bar{\psi}$ , respectively, and  $q = \sqrt{3}/2$ . Reinserting this result into the free energy yields  $f_s(\bar{\psi})$ .

The equilibrium densities of the two phases as a function of  $\epsilon$  can then be found by the common tangent construction, which is equivalent to the requirement that the chemical potential  $\mu$  and the grand potential density  $\omega = f - \mu\bar{\psi}$  must be equal in both phases,

$$\left. \frac{\partial f_s}{\partial \bar{\psi}} \right|_{\bar{\psi}_s} = \mu_s = \left. \frac{\partial f_l}{\partial \bar{\psi}} \right|_{\bar{\psi}_l} = \mu_l \equiv \mu_{eq} \quad (12)$$

$$\omega_s = f_s(\bar{\psi}_s) - \mu_s \bar{\psi}_s = \omega_l = f_l(\bar{\psi}_l) - \mu_l \bar{\psi}_l. \quad (13)$$

The solution of these equations yields the equilibrium densities as a function of temperature,  $\bar{\psi}_s^{eq}(\epsilon)$  and  $\bar{\psi}_l^{eq}(\epsilon)$ . The phase diagram of the PFC model exhibits a critical point. The parameter  $\epsilon$  plays the role of an undercooling, that is, higher  $\epsilon$  correspond to lower temperatures. Furthermore, the phase diagram is symmetric in  $\bar{\psi}$  and hence exhibits two coexistence zones. We choose for all our simulations negative values of  $\bar{\psi}$ ; for this branch of solutions the solid has a higher density than the liquid.

Finally, for values of  $\bar{\psi}$  close to zero, an additional striped (nematic) phase can exist, which is not of importance for the present work.

The one-mode ansatz gives a good approximation for the phase diagram as long as  $\epsilon$  remains small. However, it turns out that this approximation is not sufficient for our purpose since we want to determine *excess* free energies due to surfaces, which requires an excellent precision of the bulk values. Therefore, we obtained the function  $f_s(\bar{\psi})$  from the numerical solution of the free energy minimization for a periodic hexagonal pattern, and used this function to perform the common tangent construction, which leads to very precise values of  $\mu_{\text{eq}}$ ,  $\bar{\psi}_s^{\text{eq}}$ , and  $\bar{\psi}_l^{\text{eq}}$ .

The solid-liquid interfaces have been studied in detail in the PFC model and in a Ginzburg-Landau model<sup>33</sup>. The main result that is important for the present work is that for  $\epsilon$  small enough, the interfaces are smooth. That is, the amplitude of the density waves varies from the solid to the liquid over a distance  $\delta_{sl}$  that is much larger than the spacing between density peaks in the solid. This makes it possible to use a multi-scale expansion and to obtain a good approximation for the surface tension and the order-parameter profile. However, as for the bulk densities, this approximation is not precise enough for the purpose of the present work. Therefore, the surface tension is extracted from the numerical calculations as detailed below. The interface thickness  $\delta_{sl}$  is obtained from a fit of the density profile  $\bar{\psi}_x(y)$  (the density averaged over the  $x$  direction, which is parallel to the interface) with a hyperbolic tangent,

$$\bar{\psi}_x(y) = \frac{\bar{\psi}_s^{\text{eq}} + \bar{\psi}_l^{\text{eq}}}{2} + \frac{\bar{\psi}_s^{\text{eq}} - \bar{\psi}_l^{\text{eq}}}{2} \tanh\left(\frac{y}{\delta_{sl}}\right), \quad (14)$$

as shown in Fig. 1. For  $\epsilon = 0.1$  (which is used in all the simulations in this work), a value of  $\delta_{sl} \approx 12.5$  is obtained.

## B. Numerical methods

The standard equation of motion of the PFC model is<sup>19,20</sup>

$$\begin{aligned} \partial_t \psi &= \nabla^2 \left( \frac{\delta \mathcal{F}}{\delta \psi} \right) \\ &= (1 - \epsilon) \nabla^2 \psi + 2 \nabla^4 \psi + \nabla^6 \psi + \nabla^2 \psi^3, \end{aligned} \quad (15)$$

which reflects the fact that the density field is a locally conserved quantity. This equation can be efficiently solved by using a semi-implicit pseudospectral formulation, as detailed in Appendix A.

However, for the purpose of finding the equilibrium states, this is not an efficient method. The reason is that the solid and the liquid have different densities, which have to be adjusted to their equilibrium values in the course of the simulation. Since Eq. (15) implies that mass is transported by diffusion only, the equilibration time scales as the square of the system size. Instead, a more

rapid numerical scheme can be used, in which  $\psi$  is treated as a *locally* non-conserved order parameter, while *global* mass conservation is ensured by a Lagrange multiplier. The advantage of this “nonlocal” method is that the mass can be transported faster since it can be taken at some space point and placed at another, as favored by the free energy.

The equation of motion for the nonlocal dynamics is derived in Appendix A and can be written as

$$\begin{aligned} \partial_t \psi &= -\frac{\delta \mathcal{F}}{\delta \psi} + \mu \\ &= [(\epsilon - 1) - 2 \nabla^2 - \nabla^4] \psi - \psi^3 + \mu, \end{aligned} \quad (16)$$

where the Lagrange multiplier  $\mu$  is obtained as

$$\mu = \frac{1}{L_x L_y} \int [(1 - \epsilon) \psi(\vec{x}) + \psi^3(\vec{x})] d\vec{x}, \quad (17)$$

where  $L_x$  and  $L_y$  are the side lengths of the rectangular simulation box. The Lagrange multiplier is the thermodynamic chemical potential of the system. In the scheme outlined above, the total mass of the system is conserved, and the chemical potential evolves with pseudo-time until it reaches its stationary equilibrium value.

Finally,  $\mu$  can also be fixed, and the constraint of global mass conservation released. This corresponds to a situation described by the grand canonical ensemble, and  $\mu$  is the externally imposed chemical potential. The equilibrium state can be reached even faster in this way since each point of the system can directly exchange mass with the “mass reservoir”. The equation of motion is identical to Eq. (16), except that now  $\mu$  is an external parameter and independent of time. This method is much faster than the others and will be used for almost all of the simulations presented below. However, it should be emphasized that it is not suitable to simulate isolated solid-liquid interfaces or two-phase states within the co-existence region, since for such states the density  $\bar{\psi}$  is not a unique function of  $\mu$ . Such states have therefore to be calculated with fixed total mass.

Here we neglect the effect of thermal fluctuations that is traditionally incorporated in the PFC model through the addition of a Langevin noise term in the evolution equation for the density field, with the amplitude of the noise determined by a standard fluctuation-dissipation relation<sup>19,20,38</sup>. This choice is motivated by the fact that we focus primarily on computing quantitatively the excess interfacial free energies of dry and wet equilibrium grain-boundary states that correspond to stable or metastable free-energy minima. This requires an accurate computation of the free energy of the system that is readily obtained from a static crystal density field using the “bare” free-energy functional defined by Eq. (7), but that is considerably more difficult to obtain when noise is present. In the latter case, the additional entropy generated by the fluctuations of the crystal density field needs to be computed explicitly to obtain a “renormalized” free-energy functional, which is needed

to compute in a thermodynamically self-consistent way the disjoining potential. While such a computation is in principle possible (although it would require long simulations for statistical averaging) it appears unnecessary for the computation of static equilibrium properties since the bare free-energy functional is derived from a mean-field classical density-functional theory framework that already contains the effect of microscopic fluctuations on the atomic scale. From this fundamental viewpoint, noise in the PFC model can only be meaningfully defined in the framework of a long-wavelength hydrodynamic theory where it only acts on length scales larger than the correlation length. PFC simulations with noise in this hydrodynamic limit and without noise should give essentially identical results as far as static equilibrium properties are concerned. One possible exception is the case where different grain-boundary states (corresponding to the isolated and paired liquid pool structures already mentioned in Sec. I C) are separated by small free-energy barriers. While such barriers are present in the bare free-energy landscape studied here, they could potentially be reduced or eliminated in the renormalized landscape due to frequent thermally activated transitions between these two states.

The boundary conditions have to be treated with some care. The solid phase in the PFC model has a periodic structure and can support strain through a variation of the wavelength with respect to the equilibrium value. However, this variation alters the free-energy density of the solid phase. In order to recover the correct equilibrium values in the thermodynamic limit of large system size, it is important to ensure that the solid far from the grain boundaries is free from strain. Since we use periodic boundary conditions in both  $x$  and  $y$  directions, the size of the simulation box has to be carefully adjusted to contain exactly an integer number of unstrained unit cells; this is detailed in Appendix B.

The initial conditions used to simulate grain boundaries are two solid slabs which are rotated by an angle  $\Theta = \theta/2$  in opposite directions. The solid is created using the density field in the one-mode approximation  $\psi_s(x, y)$  as given in Eq. (10). The solids are initially separated by macroscopically large liquid films, where  $\psi = \bar{\psi}_l$ . Note that due to the periodic boundary conditions and the symmetries, there are always two equivalent grain boundaries in the system. To obtain “dry” grain boundaries,  $\bar{\psi}$  (or  $\mu$  in the case of grand canonical simulations) is chosen to be within the solid phase. Then, in the beginning of the simulations, the liquid rapidly solidifies and the grain boundary builds up. Before extracting the grain-boundary properties, the system is evolved for a much longer time. The approach to equilibrium can be monitored by determining the maximum difference between the local chemical potential given by Eq. (8) and the thermodynamic chemical potential (the Lagrange multiplier in Eq. (17) for conserved total mass, or the externally imposed value for grand-canonical simulations).

For  $\Theta = 0$ , a single crystal is obtained after the liquid has disappeared. Due to the symmetry of the hexagonal structure, this happens also when  $\Theta = 30^\circ$ , but the two configurations differ. In the former case, the close-packed rows of density peaks are aligned with the  $x$  axis and hence parallel to the initial liquid layer, whereas in the second case, they are aligned with the  $y$  direction and hence perpendicular to the liquid layer. Therefore, configurations with  $\Theta$  close to  $0$  or  $30^\circ$  correspond to symmetric tilt grain boundaries of inclination  $\phi = 0^\circ$  and  $\phi = 30^\circ$ , respectively. Furthermore, the misorientation is given by  $\theta = 2\Theta$  for  $\phi = 0^\circ$ , but by  $\theta = 60^\circ - 2\Theta$  for  $\phi = 30^\circ$ . We recover of course the well-known fact<sup>36</sup> that there are two equivalent descriptions for each grain boundary. In the following, we will investigate the whole range of angles  $0 < \Theta < 30^\circ$ , which includes low-angle grain boundaries of both inclinations.

### III. DETERMINATION OF THE GRAIN-BOUNDARY PROPERTIES

#### A. General framework

Experiments and MD simulations are mostly carried out at constant temperature, pressure, and total number of atoms. Therefore, the appropriate thermodynamic potential is the Gibbs free energy. In the PFC model, the starting point is a Helmholtz free-energy functional. Simulations carried out at fixed total mass correspond hence to constant temperature (here,  $\epsilon$ ), volume, and particle number, and lead to a minimization of the functional  $\mathcal{F}$ . In contrast, if the constraint on the total mass is relaxed and the chemical potential is fixed, we have constant temperature, chemical potential and volume, and the relevant thermodynamic potential which is minimized by the dynamics is the grand potential,

$$\Omega = \mathcal{F} - \mu \int_V \psi. \quad (18)$$

Like the Gibbs free energy, it depends on two intensive variables (temperature and chemical potential). We will formulate all the subsequent discussion in terms of the grand potential, and briefly discuss below how our methods and results can be translated to the  $(N, p, T)$  ensemble and the Gibbs free energy.

The grand potential depends on the intensive variables  $T$  (here,  $\epsilon$ ) and  $\mu$ . We will assume in the following developments that  $T$  is kept constant and that only  $\mu$  is varied. The motivations for this choice will be discussed below. Since we have chosen the side of the PFC phase diagram where the solid has a higher density than the liquid, increasing the chemical potential with respect to the coexistence value favors the solid phase. Therefore, increasing the chemical potential is analogous to decreasing the temperature.

The grain boundary is described as a thin film of liquid sandwiched between two solids, and the total grand

potential of this two-phase system is written as

$$\Omega(\mu) = L_x [(L_y - w)\omega_s(\mu) + w\omega_l(\mu) + 2\gamma_{sl} + V(w)], \quad (19)$$

where  $L_x$  is the length of the grain boundary contained in the box (the equivalent of the total surface of grain boundary in three dimensions),  $L_y$  is the system size in the direction normal to the grain boundary,  $w$  is the thickness of the liquid film, and  $\omega_s(\mu)$  and  $\omega_l(\mu)$  are the grand potential densities of the bulk solid and liquid, respectively. Equation (19) is the direct analog in the grand canonical ensemble of Eq. (1) in the Gibbs ensemble.

As already described in Sec. I, the last two terms in the brackets on the right-hand side describe the excess grand potential that is due to the presence of surfaces:  $\gamma_{sl}$  is the surface free energy of an isolated solid-liquid interface, and  $V(w)$  is the *disjoining potential*, which describes the fact that two solid-liquid interfaces start to interact when the distance between them becomes comparable to the range of the interatomic potentials. Since  $V(w)$  describes the interaction between interfaces, it has to tend to zero for well-separated interfaces,  $V(w) \rightarrow 0$  when  $w \rightarrow \infty$ . For the form of the disjoining potential that has been assumed in the sharp-interface picture in Eq. (2), a distinction can be made between “attractive” grain boundaries for which  $\gamma_{gb}^0 - 2\gamma_{sl} < 0$  (one grain boundary is more favorable than two solid-liquid interfaces), and “repulsive” or “wet” grain boundaries for which the opposite is true.

This terminology can be further motivated by defining the *disjoining pressure*  $\Pi$ , frequently used in the physics of wetting and thin liquid films<sup>18</sup>,

$$\Pi = -\frac{1}{L_x} \frac{\partial \Omega}{\partial w} = \omega_s - \omega_l - V'(w). \quad (20)$$

The disjoining pressure has two contributions. The first is of thermodynamic origin and changes sign at the melting point. Indeed, the grand potential density can be expanded in  $\mu$  around the melting point, which yields

$$\omega_s - \omega_l \approx -(\bar{\psi}_s^{\text{eq}} - \bar{\psi}_l^{\text{eq}})(\mu - \mu_{\text{eq}}), \quad (21)$$

where we have used the identity  $\partial\omega/\partial\mu = -\bar{\psi}$  and the fact that  $\omega_s = \omega_l$  at coexistence. The second contribution in the disjoining pressure arises from the interaction of the interfaces. For the simple exponential form of the disjoining potential given in Eq. (2), its sign depends only on the quantity  $\Delta\gamma = \gamma_{gb}^0 - 2\gamma_{sl}$ .

These considerations yield an alternative and quite intuitive picture of the phenomena already discussed in Sec. I. When both contributions of the disjoining pressure are negative ( $\mu > \mu_{\text{eq}}$ , attractive interfaces) the film thickness vanishes ( $w = 0$ ). When both are positive ( $\mu < \mu_{\text{eq}}$ , repulsive interfaces), the film thickness becomes infinite. The more interesting scenarios arise when the two contributions are of opposite signs: for attractive interfaces, metastable solids separated by a thin liquid film can exist for  $\mu^* < \mu < \mu_{\text{eq}}$ . For repulsive interfaces, finite liquid films exist for  $\mu_b > \mu > \mu_{\text{eq}}$

since the repulsion between interfaces competes with the thermodynamic force “pushing” the two solids together. Here,  $\mu^*$  and  $\mu_b$  are the equivalents of the “breaking” and “bridging” temperatures  $T^*$  and  $T_b$  defined in Sec. I.

We would like to point out that the notations used in Eq. 2 can easily lead to confusion because of the use of the “grain-boundary energy”  $\gamma_{gb}^0$  in the expression for  $\Delta\gamma$ . Indeed, the grain-boundary energy of *any* grain boundary, be it “dry” or “wet”, is defined as the total excess grand potential per unit length of grain boundary with respect to a *single-phase solid*. Therefore, the grain-boundary energy is

$$\begin{aligned} \gamma_{gb}(\mu) &= \frac{\Omega(\mu) - L_x L_y \omega_s(\mu)}{L_x} \\ &= (\omega_l - \omega_s)w_{\text{eq}}(\mu) \\ &\quad + 2\gamma_{sl} + V(w_{\text{eq}}(\mu)), \end{aligned} \quad (22)$$

where the equilibrium film thickness for given chemical potential,  $w_{\text{eq}}(\mu)$ , is obtained from the condition that  $w_{\text{eq}}$  minimizes the grand potential (which corresponds to a vanishing disjoining pressure),

$$V'(w_{\text{eq}}(\mu)) = \omega_s(\mu) - \omega_l(\mu). \quad (23)$$

It can be easily seen that  $\gamma_{gb} = \gamma_{gb}^0$  only when  $w = 0$ . It should be emphasized that Eq. (22) is completely general, and not limited to the special case of an exponential disjoining potential. This relation, which shows that the grain-boundary energy and the disjoining potential are not independent, can actually be exploited to determine the disjoining potential, as will be detailed below.

## B. Liquid film thickness

To proceed, we need a way to extract the liquid film thickness from our simulation data. When the two solid-liquid interfaces are well separated, it is easy to define a film thickness by the distance between the midpoints of the diffuse interfaces. However, this definition becomes obsolete when the diffuse interfaces overlap. Another definition is needed; we choose here to use a Gibbs construction.

When the liquid film is macroscopically large (that is, the separation between the two solid-liquid interfaces is much larger than the intrinsic interface width), the interfaces do not interact (the disjoining pressure vanishes) and we are in the case of two-phase coexistence, which implies that  $\mu = \mu_{\text{eq}}(\epsilon)$ . The volume fractions of liquid and solid are related to the total mass of the system by the lever rule. For a one-dimensional system of length  $L_y$  and a film of thickness  $w$ , we have

$$\bar{\psi} L_y = \bar{\psi}_l w + \bar{\psi}_s (L_y - w). \quad (24)$$

with  $\bar{\psi}_l = \bar{\psi}_l^{\text{eq}}$  and  $\bar{\psi}_s = \bar{\psi}_s^{\text{eq}}$ .

This is no longer valid when the interfaces interact: the disjoining pressure modifies the equilibrium chemical potential. However, volume fractions can still be defined starting from the consideration that the solid is a



bulk phase which occupies a macroscopic volume. Consequently, the relation between its density and chemical potential is the same as that for a homogeneous solid. In contrast, the “liquid” film is microscopic, and hence this region does not have the properties of a bulk liquid. This is illustrated in Fig. 1, where we show a numerically calculated equilibrium state together with a plot of the density averaged over the direction parallel to the grain boundary. The density exhibits a “dip” and approaches the value of the liquid when the film thickness is relatively large. It exhibits an oscillatory behavior for more “dry” grain boundaries, but the average density in the grain-boundary region is still different from the one in the bulk solid.

This density change in the grain-boundary region can be exploited to define a film thickness. An *excess mass* per unit length of grain boundary can be defined by subtracting the mass of the homogeneous solid at the same chemical potential from the actual mass contained in the system,

$$\psi_{\text{exc}}(\mu) = L_y [\bar{\psi} - \bar{\psi}_s(\mu)]. \quad (25)$$

Furthermore, it is easy to obtain the density of a bulk liquid at the same chemical potential,  $\bar{\psi}_l(\mu)$  from the curve of  $f_l(\bar{\psi})$ . Then, the film thickness can be defined by the requirement that the density difference of the bulk phases times the film thickness is equal to the excess mass,

$$w [\bar{\psi}_l(\mu) - \bar{\psi}_s(\mu)] = \psi_{\text{exc}}(\mu). \quad (26)$$

Putting these two equations together, we obtain again the lever rule, but this time with  $\bar{\psi}_s(\mu)$  and  $\bar{\psi}_l(\mu)$  instead of the coexistence values. With this definition, the film thickness can be extracted with good precision from simulations either at fixed total mass ( $\mu$  is measured in the simulation) or at fixed chemical potential (the total density  $\bar{\psi}$  is measured).

### C. Grain-boundary energy and disjoining potential

It turns out that the direct numerical determination of the grain-boundary energy requires some care. It is defined as the excess of grand potential. Contrary to the mass excess defined above, the straightforward method of subtracting the grand potential of a homogeneous bulk solid from the total grand potential of the simulated system leads to large numerical errors. This is most likely due to the evaluation of the gradient contributions in the free energy. A more precise method is to exploit the dependence on system size. By dividing Eq. (19) through  $L_x L_y$  and using the definition of the grain boundary energy, we obtain that the total grand potential density varies with system size at fixed chemical potential as  $\omega = \omega_s + \gamma_{gb}/L_y$ . The grain-boundary energy can therefore be obtained from a plot of  $\omega$  versus the inverse system size.

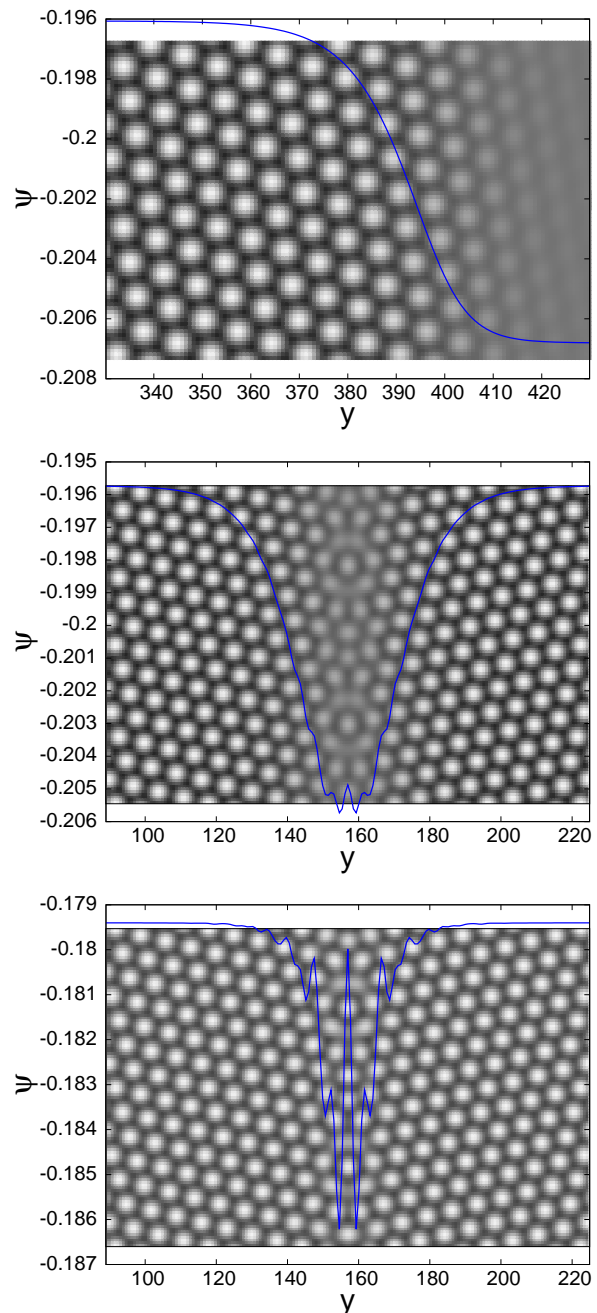


FIG. 1: (Color online) Density profiles of solid-liquid interface and grain boundaries. The complete two-dimensional density field  $\psi(x, y)$  is shown. The superimposed line gives, for any point along the direction normal to the grain boundary, the value of the density averaged over the direction parallel to the grain boundary ( $\bar{\psi}_x(y) = (1/L_x) \int \psi(x, y) dx$ ). Top: Solid-liquid interface,  $\theta = 21.8^\circ$ . Middle: Solid-solid interface close to the melting point,  $\bar{\psi} = -0.1980$ ,  $\theta = 32.2^\circ$ . Bottom: Solid-solid interface far from the melting point,  $\bar{\psi} = 0.180$ ,  $\theta = 32.2^\circ$ .

A second, and slightly simpler way, to obtain the grain boundary energy is to perform simulations at a fixed total density  $\bar{\psi} = \bar{\psi}_0$  and to use the free energy density, which can be directly obtained from the simulations. Indeed, since the density in the grain boundary is different from that in the bulk, for a fixed total density and length of grain boundary, the bulk density in the solid  $\bar{\psi}_s$  (and therefore also the chemical potential) vary with the system size. In the limit  $L_y \rightarrow \infty$ , the bulk density  $\bar{\psi}_s$  tends to  $\bar{\psi}_0$  and the chemical potential tends to the value corresponding to a solid at that density. Using the result obtained above,  $\omega = \omega_s + \gamma_{gb}/L_y$ , and the definition  $\omega = f - \mu\bar{\psi}$  we obtain

$$f = f_s(\bar{\psi}_s) - \mu(\bar{\psi}_s - \bar{\psi}_0) + \frac{\gamma_{gb}}{L_y}. \quad (27)$$

Expanding  $f_s$  in  $\bar{\psi}$  around  $\bar{\psi}_0$ , using that  $\partial f/\partial \bar{\psi} = \mu$ , and inserting the result in the above equation, all the terms involving  $\mu$  cancel out, and finally we obtain

$$f = f_s(\bar{\psi}_0) + \frac{\gamma_{gb}}{L_y}. \quad (28)$$

Therefore, we determine the excess grand potential by performing simulations at fixed  $\bar{\psi}_0$  and calculating the free energy directly from the free energy functional. Note that  $\gamma_{gb}$  depends on  $\mu$  and hence also varies with system size. However, this gives rise to terms in  $f$  that are of order  $1/L_y^2$  and should therefore be small. A plot of the total free-energy density versus  $1/L_y$ , as shown in Fig. 2, is indeed well fitted by a straight line. Therefore, we can extract the slope and intercept, which correspond to  $\gamma_{gb}$  and to the free-energy density in the thermodynamic limit, respectively. A numerical error can also be estimated from the fit if more than two different lengths are simulated. The same procedure is also used to determine the solid-liquid surface tensions. For this, it is sufficient to choose an average density which leads to macroscopically large liquid films.

The disjoining potential can then be obtained in two ways. We remark that  $\omega_l - \omega_s$  is a function of  $\mu$  only, and thus  $V'(\mu)$  is a known function of  $\mu$  which depends only on bulk thermodynamics. The extraction of the liquid layer thickness from the simulations yields  $w_{eq}(\mu)$ . The two can be combined to yield  $V'(w)$  which can then be integrated to  $V(w)$ . Alternatively, once the grain-boundary energy is calculated, Eq. (22) can be used to obtain  $V(\mu)$ , which can again be combined with  $w(\mu)$  to yield  $V(w)$ . While this second approach avoids a numerical integration, it is also more costly since for each value of the grain-boundary energy several simulations with different system sizes have to be performed.

#### D. Thermodynamic consistency

It is useful to comment here on two important points with regards to the thermodynamics of interfaces and

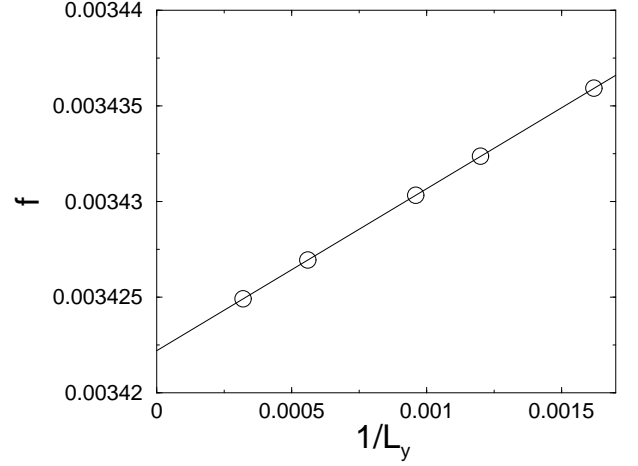


FIG. 2: Symbols: Free energy densities  $f$  of systems with the same misorientation and average densities  $\bar{\psi}$  but different lengths  $L_y$  perpendicular to the grain boundary, plotted versus  $1/L_y$ . Line: Linear fit to the data. The slope gives twice the grain-boundary energy, where the factor of 2 is due to the fact that in periodic systems there are always two grain boundaries. In this example,  $\epsilon = 0.1$ ,  $\bar{\psi} = -0.1$ , and the misorientation is  $\theta = 6^\circ$ .

grain boundaries. The first is that with our definition of the film thickness, the disjoining potential and the grain-boundary energy are entirely thermodynamically consistent. To show this, let us first remark that Eq. (22) for the grain-boundary energy formally depends on two variables,  $\mu$  and  $w$ . Taking the differential of this equation, we find

$$\begin{aligned} d\gamma_{gb} &= [\omega_l - \omega_s + V'(w)] dw + w \left[ \frac{\partial \omega_l}{\partial \mu} - \frac{\partial \omega_l}{\partial \mu} \right] d\mu \\ &= -\Pi dw - \psi_{exc} d\mu, \end{aligned} \quad (29)$$

where we have used the definitions of  $\Pi$  and  $w$  and the fact that  $\partial \omega/\partial \mu = -\bar{\psi}$  to obtain the second equality. It is clear that the film thickness  $w$  plays, for the excess free energy, the same role as the volume in bulk thermodynamics. Furthermore, since at equilibrium the disjoining pressure vanishes,  $\Pi = 0$ , the variation of the grain-boundary energy is consistent with the fundamental definition of interfacial excess quantities<sup>39</sup>. Indeed, since  $\gamma_{gb}$  is an excess of grand potential, we can write

$$\gamma_{gb} = f_{exc} - \mu\psi_{exc}, \quad (30)$$

where  $f_{exc}$  is the excess free energy; differentiation with respect to  $\mu$  yields

$$\frac{\partial \gamma_{gb}}{\partial \mu} = -\psi_{exc}. \quad (31)$$

As a corollary, once a value of  $\gamma_{gb}$  is known for a single value of  $\mu$ , the curve  $\gamma_{gb}(\mu)$  can be obtained by integrating the function  $-\psi_{exc}(\mu)$  extracted from the simulations. Furthermore, formally the grain-boundary energy

can also be obtained by keeping  $\mu$  fixed and integrating the “mechanical work”  $-\Pi dw$  over  $w$ , noticing that the disjoining pressure is non-zero if  $w \neq w_{\text{eq}}$ . This procedure, however, cannot be carried out in practice since the configurations with  $\Pi \neq 0$  are not equilibrium states and hence cannot be obtained in simulations.

The second remark concerns the generalization of our definition and procedures to other variables and ensembles. The various relationships between  $w$ ,  $V(w)$ , and  $\gamma_{gb}$  obtained above all make use of the fact that the film thickness has been defined by a Gibbs construction using the interface excess of the density, which is the extensive quantity conjugate to the externally controlled intensive variable  $\mu$ . Equivalent constructions can of course be performed with other pairs of variables. For instance, in their lattice-gas study, Kikuchi and Cahn kept the chemical potential constant and varied the temperature, while they defined the thickness of the liquid layer by the excess of entropy<sup>14</sup>. Similarly, in the  $(N, p, T)$  ensemble, a film thickness can be defined *via* the excess entropy for varying temperature, or *via* the excess volume for varying pressure. Since, in this ensemble, the volume is no longer constant, instead of volume densities as above, quantities normalized by the particle number have to be used. Nevertheless, following the ideas in Ref.<sup>39</sup> to treat this change in normalization, all the relations given above can be translated without difficulties.

A more complex situation arises if both the chemical potential and the temperature (here,  $\epsilon$ ) are allowed to vary. For clarity of exposition, we use in the remainder of this subsection the temperature  $T$  instead of the dimensionless quantity  $\epsilon$ . The definition of the grain-boundary energy and its variation become

$$\gamma_{gb} = e_{\text{exc}} - T s_{\text{exc}} - \mu \psi_{\text{exc}} \quad (32)$$

$$d\gamma_{gb} = -\Pi dw - s_{\text{exc}} dT - \psi_{\text{exc}} d\mu, \quad (33)$$

respectively, where  $e_{\text{exc}}$  and  $s_{\text{exc}}$  are the interfacial excesses of the internal energy and the entropy, respectively. Since  $\gamma_{gb}$  as well as all the other excess quantities are defined as excesses with respect to a bulk thermodynamic potential that depends on  $\mu$  and  $T$ , they are all state functions, that is, unique functions of the two intensive variables  $\mu$  and  $T$ . The same is true of the film thickness  $w$ , which is defined through an interfacial excess quantity.

In contrast, the disjoining potential is *not* a state function. This is easy to see when considering the equilibrium condition for the film thickness, Eq. (23): its right-hand side,  $\omega_s - \omega_l$ , now depends on the two variables  $\mu$  and  $T$ , which implies that  $V'(w)$  has the same dependency. If this is to be integrated to a function of a single variable  $w$ , a direction in the space spanned by  $\mu$  and  $T$  has to be specified. Another way to state the same fact is to remark that in Eq. (22),  $\gamma_{gb}$  depends on the two independent variables  $\mu$  and  $T$ , whereas the “reference value”  $2\gamma_{sl}$  depends only on one independent variable, since  $\gamma_{sl}$  is only defined on the coexistence line in the phase diagram,  $\mu_{\text{eq}}(T)$ . For a given point away from this line, where  $\gamma_{gb}$  is still defined,  $V$  can be defined only

if a reference point on the coexistence line is specified. This amounts to specifying the path in the state space that is to be followed. In the developments above, we have supposed a particularly simple path, namely, a constant value for one of the variables. It would be possible to extract from our PFC model disjoining potentials at constant pressure or at constant density: for both cases, the bulk equation of state for the solid (which can be obtained from  $f_s(\mu, T)$ ) fixes a relation between  $\mu$  and  $T$ , and  $V'(w)$  can be integrated along this path. Note, however, that this procedure requires the calculation of both the excess mass and the excess entropy.

In summary, the definition of the disjoining potential is only meaningful if the corresponding path in thermodynamic state space is specified, and the knowledge of a single disjoining potential yields only a partial knowledge about the premelting transition. The more general quantity is the grain-boundary energy, which is the thermodynamic potential for the interfacial excess quantities. If its dependence with respect to the two intensive variables is known, all the possible disjoining potentials can be easily extracted using Eq. (22).

### E. Choice of simulation parameters

Having the discussion of Sec. III D in mind, we need to choose a particular path in the state space to investigate the disjoining potential. It would be possible to approach the melting transition from the solid side for a fixed chemical potential by decreasing  $\epsilon$ . However, extracting the excess entropy is far more delicate than extracting the excess mass. Therefore, in the following we prefer to keep  $\epsilon$  fixed to 0.1 (a value that has been obtained for the equilibrium solid-liquid interfaces in pure iron with body-centered-cubic crystal ordering<sup>33,34</sup>) and to explore the melting transition by varying the chemical potential  $\mu$ .

For the subsequent presentation of the results, we will use the following rescaled variables:

$$\Delta = \frac{\bar{\psi} - \bar{\psi}_s^{\text{eq}}}{\bar{\psi}_s^{\text{eq}} - \bar{\psi}_l^{\text{eq}}}. \quad (34)$$

This corresponds to a supersaturation. Furthermore, we define a scaled chemical potential by

$$u = \frac{\mu_{\text{eq}} - \mu}{\left. \frac{\partial \mu}{\partial \psi_s} \right|_{\bar{\psi}_s^{\text{eq}}} (\bar{\psi}_s^{\text{eq}} - \bar{\psi}_l^{\text{eq}})}, \quad (35)$$

where the sign is chosen to stress the analogy between  $u$  and a temperature<sup>40</sup>: for  $u < 0$  ( $u > 0$ ), the solid (liquid) is the favored phase. For  $\mu$  close to the coexistence value, the numerator can be expanded in  $\bar{\psi}$ , which yields  $u \approx -\Delta$ . We list in Table I the values of all the quantities needed for this scaling. Furthermore, we will often rescale the grain-boundary energy by  $2\gamma_{sl}$ , and lengths by  $a$ , the lattice spacing of the hexagonal crystal. The values of these quantities are also given in Table I.

TABLE I: Numerical values of various quantities needed to scale the density, chemical potential, grain-boundary energy, and lengths, for  $\epsilon = 0.1$ .

Quantity	Symbol	Value
Solid density at coexistence	$\bar{\psi}_s^{\text{eq}}$	-0.19696406
Liquid density at coexistence	$\bar{\psi}_l^{\text{eq}}$	-0.2068060
Chemical potential at coexistence	$\mu_{\text{eq}}$	-0.19497015
Slope of the curve $\mu$ versus $\bar{\psi}_s$	$\partial\mu/\partial\bar{\psi}_s$	0.731218
Solid-liquid surface tension ( $\times 2$ )	$2\gamma_{\text{sl}}$	0.00192
Lattice constant	$a$	$\frac{4\pi}{\sqrt{3}} \approx 7.2552$

## IV. RESULTS

### A. Structure of the grain boundaries

Our simulations reveal that there is a strong difference in behavior between high-angle and low-angle grain boundaries. In order to illustrate first a few important features, we show in Figs. 3 and 4 snapshot pictures of a high-angle and a low-angle grain boundary of inclination  $\phi = 0^\circ$ , for different values of  $u$ . Furthermore, we plot in Fig. 5 the curves of film thickness  $w$  versus scaled chemical potential  $u$  corresponding to the same two grain boundaries. We have checked that canonical and grand-canonical simulations (fixed total mass and fixed chemical potential, respectively) yield identical results for the film thickness and the grain-boundary structure.

For both high-angle and low-angle grain boundaries, the film thickness becomes negative far below the melting point. Indeed, formally, since the film thickness is defined *via* an excess mass, it does not need to remain positive. A negative film thickness corresponds to an accumulation of mass in the grain boundary instead of the depletion observed in Fig. 1. When  $u$  is increased, the film thickness becomes positive, but remains small until the vicinity of the melting point is reached. For the high-angle grain boundary, the film thickness then increases rapidly and diverges as the melting point is approached from below; this is the behavior expected for a repulsive grain boundary. In the snapshot pictures, it can be seen that the liquid film is rather homogeneous, that is, it has approximately the same width at every point.

The low-angle grain boundary depicted in Fig. 4 consists of individual dislocations separated by distances that are larger than a few lattice spacings. Here, the “liquid” first appears in the form of “pools” around the dislocations, and there is no homogeneous film of liquid. Furthermore, as the melting point is approached, a structural transition occurs: the dislocations form pairs; that is, two dislocations join and are surrounded by a common liquid pool. This transition is accompanied by a jump in the film thickness  $w$ . Furthermore, this structure can be “overheated”; that is, such states exist even for  $u > 0$ , which indicates an attractive grain boundary. The pools grow in size, thus reducing the strength of the “bridges” of solid. At a critical overheating, the bridges break, and

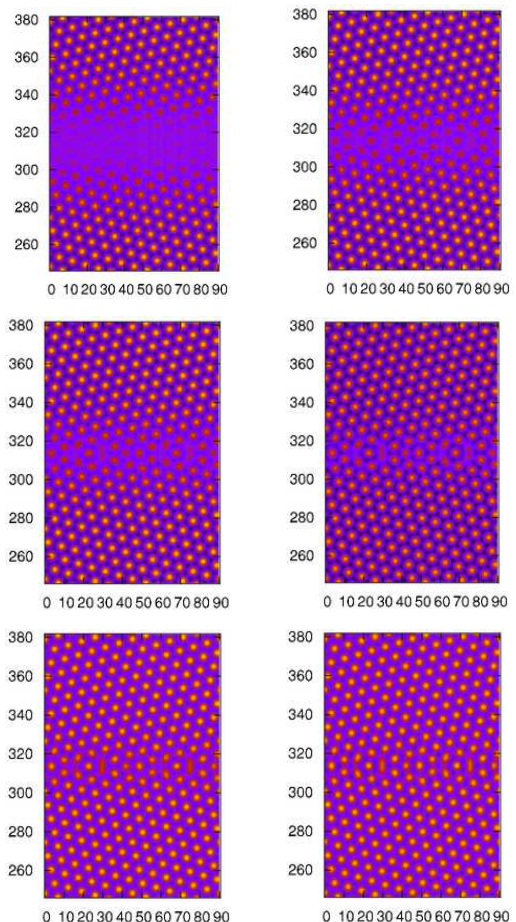


FIG. 3: (Color online) Snapshots of a high-angle grain boundary with  $\theta = 32.2^\circ$  for different values of  $u$ , which increase from bottom right to top left (see text and Fig. 5 for details). The “liquid” forms a rather homogeneous film. Only part of the simulation box is shown.

the whole system becomes liquid.

Most of the features described above – dependence of the film thickness on  $u$ , transition from attractive low-angle to repulsive high-angle grain boundaries, existence of overheated states – are also present for the symmetric tilt grain boundaries of inclination  $\phi = 30^\circ$ . However, for this inclination there is no transition from single dislocations to dislocation pairs. This transition was also not observed in the three-dimensional PFC study with bcc symmetry in Ref.<sup>26</sup>. It can hence be concluded that its occurrence depends on the detailed microscopic structure of the grain boundary.

Let us now give a more detailed description of the transition between the high-angle and the low-angle regimes. In Fig. 6 we show the curves of  $w$  versus  $u$ , for various misorientations, in the vicinity of the melting point, for the two inclinations  $\phi = 0^\circ$  and  $\phi = 30^\circ$ , respectively. We recall (see the discussion in Sec. II B) that due to the hexagonal symmetry the two curves shown for  $\phi = 0^\circ$ ,  $\theta = 32.2^\circ$  and for  $\phi = 30^\circ$ ,  $\theta = 27.8^\circ$  actually describe the



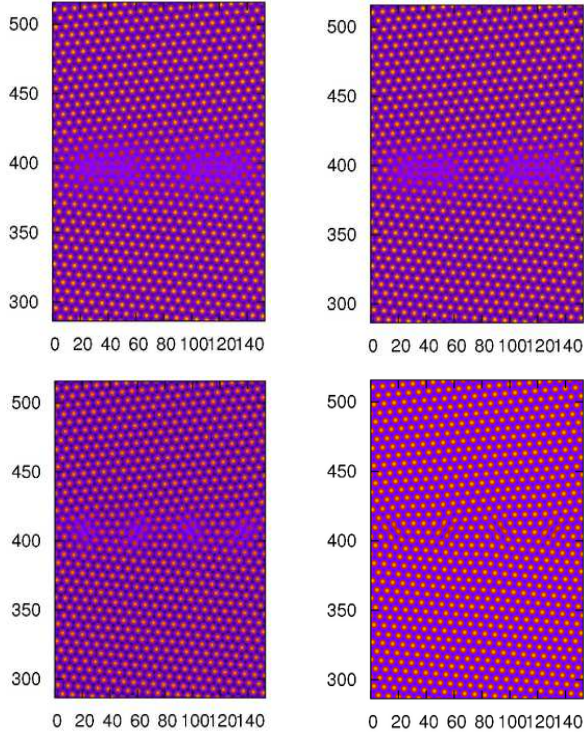


FIG. 4: (Color online) Snapshots of a low-angle grain boundary with  $\theta = 9.4^\circ$  for different values of  $u$ , which increases from bottom right to top left (see text and Fig. 5 for details). The grain boundary consists of individual dislocations and undergoes a structural transition. Only part of the simulation box is shown.

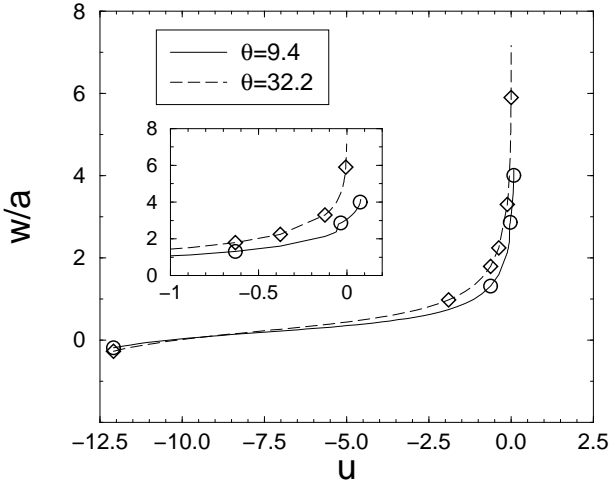


FIG. 5: Ratio of film thickness  $w$  to lattice spacing  $a$  as a function of scaled chemical potential  $u$  for two different grain boundaries. The inset shows a blowup of the vicinity of the melting point. The symbols mark the states that are depicted in the snapshot pictures in Figs. 3 and 4.

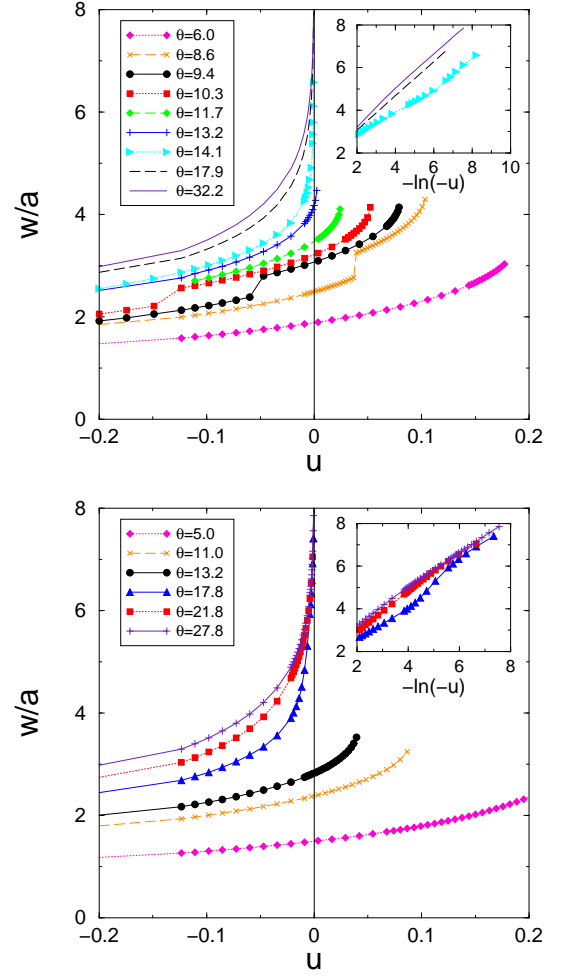


FIG. 6: (Color online) Film thickness  $w$  as a function of  $u$  for various misorientations, for symmetric tilt grain boundaries of inclination  $\phi = 0^\circ$  (top) and  $\phi = 30^\circ$  (bottom) close to the melting point. All angles are given in degrees, and a vertical line has been drawn at the melting point  $u = 0$ . Inset: Film thickness of the three largest angles versus  $-\ln(-u)$ : the divergence of the film thickness is logarithmic.

same grain boundary. All curves have been calculated by simulations at fixed chemical potential. The final state of a given run was used as initial condition for the next one at slightly different chemical potential.

The insets of Fig. 6 show the film thickness for the three largest misorientations for both inclinations, all corresponding to repulsive interfaces, versus  $-\ln(-u)$ . For large film thickness, the curves become linear, which is the dependence that is expected for an exponential disjoining potential from Eqs. (2) and (3). According to Eq. (3), the slope of this linear part is the decay length  $\delta$ . We find a value of  $\delta \approx 5.8$ , which is approximately half of the thickness of the solid-liquid interfaces  $\delta_{sl} \approx 12.5$ , and comparable to the wavelength of the dominant density waves of the hexagonal structure (which is equal to  $2\pi$  in our scaling).

It can be seen that the transition between repulsive and attractive behaviors occurs at an angle of  $\theta_c \approx 14^\circ$  for both inclinations. This transition is smooth in the sense that the critical value  $u^*$  where the solid bridges break decreases with increasing misorientation and seems to tend to zero at the transition angle without exhibiting a jump. Furthermore, the thickness of the liquid layer at the melting point,  $w_m = w(0)$ , increases with misorientation and seems to diverge continuously when  $\theta_c$  is approached from below. The precise nature of this divergence remains undetermined. Its detailed study would require simulations in a narrow range of misorientations close to the critical angle, which is quite cumbersome because of the geometrical constraints that arise from the finite size of the simulation box.

It is important to stress that this transition does *not* coincide with a structural transition of the grain boundary. The curves of  $w$  versus  $u$  for  $\theta = 32.2^\circ$  and  $\theta = 17.9^\circ$  in Fig. 6 are very similar; however, the structure of these grain boundaries is quite different. In all the snapshot pictures in Fig. 3, the grain boundary is a plane of mirror symmetry for the density field. This is not the case for  $\theta = 17.9^\circ$ : far from the melting point, this grain boundary consists of individual dislocations such as the low-angle grain boundary shown in Fig. 4. The transition from single dislocations to dislocation pairs also occurs, but far from the melting point, around  $u = -1.4$ . When the melting point is approached, a continuous transition from a state similar to the uppermost left picture in Fig. 4 to one that looks like the uppermost left picture in Fig. 3 occurs: the liquid pools around the dislocation pairs increase in size and finally merge to give rise to a fairly homogeneous film. The “liquid pools” separated by “solid bridges” are therefore present in the vicinity of the melting point both for repulsive and attractive grain boundaries.

In Fig. 6, jumps in the film thickness can be seen in the curves for  $\theta = 8.6^\circ$ ,  $9.4^\circ$ , and  $\theta = 10.3^\circ$ ; they correspond to the occurrence of the transition from single dislocations to dislocation pairs. The value of  $u$  at which this transition occurs increases with decreasing misorientation. As mentioned before, for  $\theta = 17.9^\circ$ , it occurs far below the melting point; for  $\theta = 8.6^\circ$ , it occurs only above the melting point. For an even lower misorientation,  $\theta = 6.0^\circ$ , it does not occur at all: the liquid pools around the single dislocations increase in size until the solid “bridges” between them break.

This structural transition exhibits a hysteresis. In Fig. 7 we show two curves of  $w$  versus  $u$  for  $\theta = 9.6^\circ$  that are computed in different ways. In the first, we start from a single-dislocation state at low values of  $u$  and then perform successive simulations with increasing  $u$ , taking the final state of the previous simulation as initial condition. In the second, we start from a dislocation-pair state and successively decrease the value of  $u$ . It can be seen that there exists a range of  $u$  in which both single-dislocation and dislocation-pair states are stable. This indicates that there exist at least two distinct branches

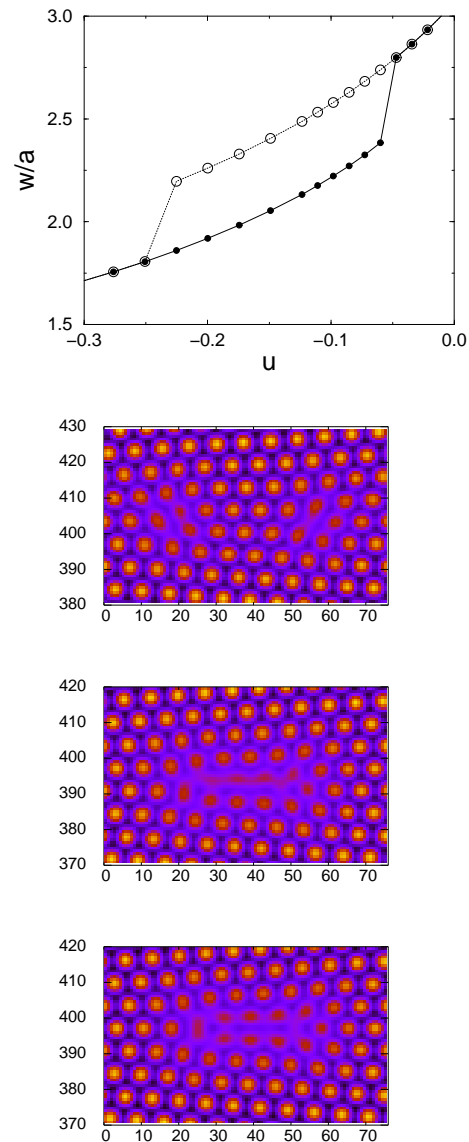


FIG. 7: Various grain-boundary states for inclination  $\phi = 0^\circ$  and misorientation  $\theta = 9.4^\circ$ . The curve  $w$  versus  $u$  exhibits a hysteresis: filled symbols are calculated with increasing  $u$  (same curve as shown in Fig. 6), and open symbols with decreasing  $u$ . The snapshot pictures show different grain-boundary states, all at  $u = -0.072$ . Top: single-dislocation state, middle: dislocation pair calculated with a single-dislocation state as initial condition, bottom: dislocation pair calculated with the initial conditions described in Sec. II B.

of grain-boundary solutions. In addition, there exist different configurations for the dislocation-pair state, as is shown in the snapshot pictures in Fig. 7: if the simulation is started from the initial conditions described in Sec. II B, the dislocation pair state exhibits a mirror symmetry with respect to the plane of the grain boundary, as also seen in the snapshots in Fig. 4. The dislocation-

pair states obtained starting from a single-dislocation state do not exhibit this symmetry. However, the size and shape of the “liquid pool” are quite similar, and the film thickness extracted from the two different configurations is identical up to the numerical precision. We have also found that in the case of the low-angle grain boundary that does not exhibit the transition ( $\theta = 6.0^\circ$ ), dislocation-pair states can be obtained starting from the initial condition in Sec. II B; they form a second branch of solutions for this misorientation.

The hysteretic nature of this transition and the dependence of the final state on the initial conditions are clear indications that the free-energy functional of the PFC model has several distinct minima which correspond to grain-boundary states of different grain-boundary energies. For low values of  $u$ , the single-dislocation states have a lower energy and the dislocation-pair states correspond to a metastable minimum, whereas the inverse is true for high values of  $u$ . Since the extraction of the grain-boundary energy is delicate, we have not pinpointed the exact value of  $u$  where the two states have equal energies. But from the general phenomenology of hysteretic transitions, it can be expected to lie approximately in the middle of the bistable range. Furthermore, since our simulations do not include thermal fluctuations, the termination of the metastable branches corresponds to the disappearance of the local metastable minimum.

The existence of metastable states raises the question of whether other grain-boundary configurations, distinct from the ones depicted in Figs. 3 to 7, might exist. We investigated this question by performing several runs with different initial conditions for numerous parameter sets. We did not find any new grain-boundary states in the vicinity of the melting point. For states far from the melting point, we have occasionally observed distinct configurations that exhibit differences in the local arrangements of the “atoms” around the dislocations and different total number of “atoms”, which is possible since, even at fixed total mass, the total number of “atoms” is not fixed in the PFC model. No further investigation of these multiple states was carried out.

The curves of  $w$  versus  $u$  for intermediate misorientations that consist of dislocation pairs exhibit a vertical slope at the “break point”. It is tempting to believe that the solution branch continues beyond that point and bends back to reach  $u = 0$  when  $w \rightarrow \infty$ . This would be expected if the state of the grain boundary can be properly described by the single variable  $w$ ; such solutions have been found in phase-field studies of grain-boundary premelting<sup>27,28</sup>. In our PFC model, these solutions cannot be obtained in simulations at constant chemical potential, since they are unstable. We have tried to obtain these states by simulations with fixed total mass. In this case, mass conservation yields a constraint on the film thickness which should stabilize these states. However, our attempts were not successful due to the occurrence of a new instability. Since there are always two distinct grain boundaries in our system due to the peri-

odic boundary conditions, a symmetry breaking can occur which leads to the formation of a “thick” and a “thin” liquid film instead of two liquid films of equal thickness. This indeed happens when the film thickness is larger than the value corresponding to the “turning point”. A simple explanation for this instability will be given below. In contrast, all the curves  $w(u)$  for low-angle grain boundaries with inclination  $\phi = 30^\circ$  as well as the curve for the lowest misorientation for  $\phi = 0^\circ$  ( $\theta = 6.0^\circ$ ) do not exhibit a turning point, but break off with a finite slope. These grain-boundary states all consist of single dislocations.

From these results it can be concluded that the mechanisms that lead to the breaking of the “solid bridges” and to the instability of the overheated solution branches depend on the detailed structure of the grain boundary. Qualitatively, the difference in behavior can be understood from geometric considerations. As mentioned above, a vertical slope at the break point would be expected for homogeneous liquid films that can be faithfully described by a single variable, the film thickness  $w$ . The elongated liquid pools surrounding the dislocation pairs are more similar to a homogeneous liquid film than the round liquid pools surrounding single dislocations. Thus, it is not surprising that the behavior of the former is closer to the one of a homogeneous film.

It is clear from the above results that the description of a grain boundary by a single variable (the thickness) is very crude. However, we have found no other obvious quantity that could play the role of a supplementary state variable. Therefore, for all the following developments we will restrict our level of description to the single variable  $w$ , leaving a more detailed investigation as a subject for further study. Also note that, in principle, a distinct grain-boundary energy and disjoining potential are associated with each of the distinct solution branches. To simplify the picture, we will ignore this fact and display in the following unique curves for the grain-boundary energy and the disjoining potential. Since the film thickness  $w$  exhibits a jump,  $V(w)$  has a “step”, and the grain-boundary energy a discontinuity in slope. These features are, however, so small that they can be hardly distinguished in the following plots.

## B. Grain-boundary energy

We calculate the grain-boundary energy as described in Sec. III C by performing simulations at fixed density  $\bar{\psi}$  for several different system sizes  $L_y$  and using Eq. (28) to extract  $\gamma_{gb}$ . In order to keep the presentation consistent, we will nevertheless discuss the results as a function of  $u$ , which can be easily obtained for given density using the curve  $\mu_s(\bar{\psi})$ . All the data shown in this subsection are for grain boundaries of inclination  $\phi = 0^\circ$ . The grain-boundary energy is plotted versus misorientation in Fig. 8 for various values of the chemical potential. Two clear tendencies can be seen. First, for any fixed

misorientation,  $\gamma_{gb}$  increases monotonously when  $u$  decreases. Second, for a fixed supersaturation,  $\gamma_{gb}$  increases monotonously with the misorientation for small angles.

The latter dependency can be well understood in terms of the Read-Shockley law<sup>36</sup>,

$$\gamma_{gb} = \frac{Ga}{4\pi\alpha(1-\sigma)}\theta [1 - \ln(2\pi\theta) + \ln(\alpha a/r_0)] , \quad (36)$$

where  $r_0$  is the core radius of the dislocations,  $a$  is the lattice constant,  $\alpha = \sqrt{3}/2$  is the ratio of the distance between close-packed planes and the lattice spacing,  $G$  is the shear modulus, and  $\sigma$  is Poisson's ratio. The elastic properties of the PFC model can be determined analytically in the one-mode approximation<sup>19,20</sup>. The resulting elastic constants are  $C_{11}/3 = C_{12} = C_{44} = (3\bar{\psi} - \sqrt{15\epsilon - 36\bar{\psi}^2})^2/75$ . The bulk modulus can then be calculated to be  $Y = 2C_{44}$  and the shear modulus  $G = C_{44}$ . Furthermore, the three-dimensional Poisson's ratio is  $\sigma = (3Y - 2G)/[2(3Y + 2G)] = 1/4$ . An estimation for the core radius,  $r_0 = a \exp(-0.5) \approx 4.4$  has also been given<sup>20</sup>. Note that we have used here the standard (three-dimensional) version of the Read-Shockley law and the elastic constants. It can be shown<sup>41</sup> that this is identical to the two-dimensional expressions given by Elder and Grant<sup>20</sup>. Furthermore, this formula differs from the standard one for cubic materials by the presence of the factors  $\alpha$ , which are due to the fact that the average distance  $d$  between dislocations is  $d \sim \alpha a / \sin \theta$  (instead of  $d \sim a / \sin \theta$  for a cubic material). It should also be emphasized that this expression is only valid for grain boundaries of inclination  $\phi = 0^\circ$ ; in the general case, several additional terms depending on the inclination angle have to be included<sup>36</sup>.

For each supersaturation, we fixed the shear modulus to its density-dependent analytical value, and performed a least-squares fit of our data to the Read-Shockley law, with  $r_0$  as the only fit parameter. Since Eq. (36) is only valid for small misorientations, for the fit only systems with  $\theta < 15^\circ$  have been included. It can be seen that the fit is excellent. In the inset, the core radius  $r_0$  obtained from the fit is shown as a function of  $u$ . It is almost constant and close to the theoretically estimated value for large values of  $|u|$ , and increases when the coexistence region is approached ( $u \rightarrow 0$ ).

It turns out that the variation of the grain-boundary energy with  $u$  will be crucial for the further discussions. We recall that this variation is directly linked to the liquid film thickness by Eqs. (31) and (26). The grain-boundary energy is shown as a function of  $u$  for three selected misorientations in Fig. 9. The symbols are values that have been directly obtained from simulations with varying system size. The full lines are obtained by integrating Eq. (31), where the integration was started from the data point at  $u = -5.674$ . It is clear that the two procedures give fully consistent results. In the inset, the data for  $\gamma_{gb}$  obtained by integration are shown in the vicinity of the melting point. It should be mentioned that direct

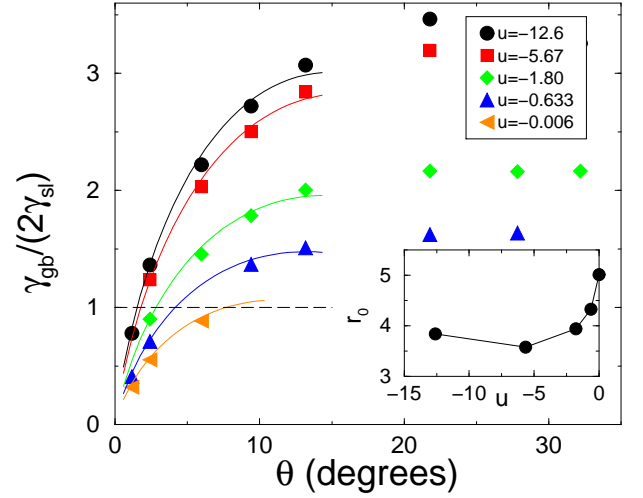


FIG. 8: (Color online) Ratio of grain-boundary energy to twice the solid-liquid free energy for grain boundaries of inclination  $\phi = 0^\circ$  as a function of the misorientation  $\theta$ , shown for different chemical potentials  $u$ . The lowest curve,  $u = -0.006$ , is very close to the melting point, while the upper curve is far inside the solid region. The lines are fits to the Read-Shockley law, Eq. (36), using the values of  $\gamma_{gb}$  for  $\theta < 15^\circ$ . The shear modulus has been fixed to the theoretical value at the corresponding chemical potential, and the only fit parameter is the dislocation core radius  $r_0$ . Inset: The core radius  $r_0$  obtained from the fits as a function of chemical potential. For comparison, the lattice constant is  $a \approx 7.255$  and the value estimated by Elder and Grant<sup>20</sup> is  $r_0 \approx 4.4$ .

calculations of the grain-boundary energy in this regime are quite difficult, since the grand potential differences between solid and liquid (and hence the driving forces) are small, so that long equilibration times are needed. The different behaviors of repulsive and attractive grain boundaries can be clearly seen. For the repulsive grain boundary (upper curve),  $\gamma_{gb}$  tends to  $2\gamma_{sl}$  from above. Since  $\psi_{exc} \sim \ln(-u)$  close to the melting point, we have  $\gamma_{gb} - 2\gamma_{sl} \sim u \ln(-u) + u$ , as expected from Eq. (5) of the sharp-interface theory. The curve has an infinite slope at  $u = 0$  (corresponding to a diverging film thickness), but the logarithmic divergence is too slow to be clearly distinguished in the figure. For the attractive grain boundaries (the lower two curves),  $\gamma_{gb}$  becomes lower than  $2\gamma_{sl}$  before the melting point is reached. It continues to decrease beyond the melting point, until the metastable solution branch ends.

As mentioned above, the dislocation core radius extracted from the fits to the Read-Shockley law is almost constant over a wide range of  $u$ . An interesting corollary of this finding is that the variation of the grain-boundary energy with chemical potential can be accounted for almost entirely by the change in the elastic constants. To illustrate this point, we show in Fig. 9 as dash-dotted lines the predictions of the Read-Shockley law with a constant value for the core radius  $r_0 = 3.75$  for the two



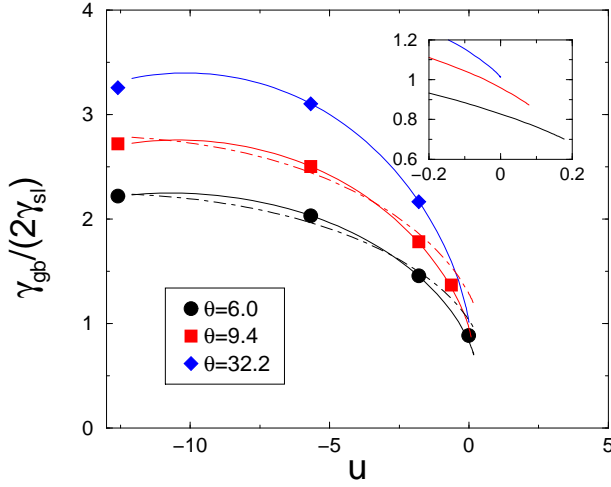


FIG. 9: (Color online) Symbols: grain-boundary energy determined from direct simulations, lines: grain-boundary energy calculated by thermodynamic integration, dash-dotted lines: prediction of the Read-Shockley law with  $r_0 = 3.75$  and elastic constants depending on  $u$ . See text for details.

lowest misorientations. Clearly, the main variation of  $\gamma_{gb}$  with supersaturation is well reproduced. The ratio of the predicted to the numerical value remains close to unity up to  $u \approx -2$  and then increases sharply to about 1.4 at the melting point. This is natural since the assumption of constant core radius breaks down. The highest misorientation shown in Fig. 9 is too large for the Read-Shockley law to be applicable. But from the figure it is clear that the variation of  $\gamma_{gb}$  with the chemical potential is very similar to the one of the low-angle grain boundaries. It is therefore reasonable to assume that this variation is also mainly controlled by the elastic constants.

### C. Disjoining potential

As outlined in Sec. III C, two methods can be used to extract the disjoining potential from the simulation data:  $V'(w)$  can be integrated using the data of  $w(\mu)$ , or  $V(w)$  can be directly deduced from the grain-boundary energy using Eq. (22). Both methods yield consistent results that are shown in Fig. 10. For the high-angle grain boundaries,  $V(w)$  decreases monotonously; it can be actually quite well described by an exponential function as in Eq. (2). In contrast, for the low-angle grain boundaries, the disjoining potential is non-monotonous: starting from a positive value at  $w = 0$ , it decreases, falls below zero and exhibits a minimum for some intermediate values of  $w$ . It then starts to increase until it reaches the point where the curve  $w(\mu)$  terminates.

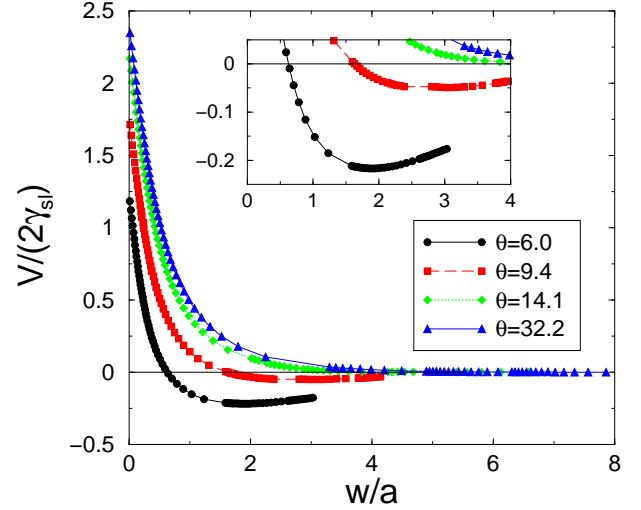


FIG. 10: (Color online) Disjoining potential for inclination  $\phi = 0^\circ$  and various misorientations (inset: detailed view of the region around the minimum). The angles are given in degrees.

## V. DISCUSSION

It is instructive to discuss some aspects of our above results in more detail and to compare them with the predictions of the sharp-interface theory. Three questions are of particular interest: what is the interpretation of the non-monotonous disjoining potentials, what determines the critical angle for the attractive-to-repulsive transition, and what can be said about the overheated grain boundaries and about transitions between different grain-boundary states?

The shape of the disjoining potential for low-angle grain boundaries can obviously not be described by the simple exponential form of Eq. (2). This potential corresponds to a short-range repulsion, but a long-range attraction. We have not found a simple analytical formula for this potential; however, a few of its properties can be readily understood. For instance, Eq. (20) tells us that  $V'(w) = 0$  implies  $\omega_s = \omega_l$ , which is only the case for  $\mu = \mu_{eq}$  ( $u = 0$ ). The minimum of the curve  $V(w)$  corresponds therefore to the intersection of the curves  $w(u)$  with the  $u = 0$  axis in Fig. 6. Since Eq. (22) yields, for  $\omega_s = \omega_l$ ,  $V(w) = \gamma_{gb} - 2\gamma_{sl}$ , this implies that the depth of the potential well is given by the difference of the grain-boundary energy *at the melting point* and twice the solid-liquid free energy. Furthermore, the value  $V(0)$  corresponds to the grain-boundary energy of a completely dry grain boundary  $\gamma_{gb}^0$ . The height of the “repulsive part” of the disjoining potential is therefore given by the difference between this value and the grain-boundary energy at the melting point. Any system in which the grain-boundary energy increases with decreasing homologous temperature will therefore exhibit a repulsive part in the

disjoining potential, even if the grain-boundary is attractive at the melting point. In addition, from Eq. (31) and Eq. (23) it is easily seen that the variation of the grain-boundary energy with  $u$  is proportional to the negative of the liquid film thickness. Therefore, the disjoining potential is repulsive below the melting point for *any* grain boundary that exhibits a finite film thickness.

It is also easy to show that the points where the curve  $w(\mu)$  exhibits a vertical tangent correspond to an inflection point in the potential  $V(w)$ . For this, it is sufficient to take the derivative with respect to  $w$  of Eq. (23), which yields

$$\begin{aligned} V''(w) &= \left( \frac{\partial \omega_s}{\partial \mu} - \frac{\partial \omega_l}{\partial \mu} \right) \frac{d\mu}{dw} \\ &= (\bar{\psi}_l - \bar{\psi}_s) \frac{d\mu}{dw}. \end{aligned} \quad (37)$$

The sign of the second derivative of the disjoining potential is hence determined by the derivative  $d\mu/dw$ , which is zero at the turning point of  $w(\mu)$ . As a consequence,  $V(w)$  is concave for large values of  $w$ . This yields a simple explanation for the instability that leads to a symmetry breaking between the two grain boundaries in the simulation box, which was described in Sec. IV A: at fixed density, the sum of the two film thicknesses  $w_1$  and  $w_2$  is approximately fixed by the lever rule. If  $w_1 = w_2 = w$ , and  $w$  is located in the concave part of the potential, the system can lower its total energy by making one film wider and the other one thinner.

Let us now consider the transition from attractive to repulsive grain boundaries. As discussed in Sec. I, the sharp-interface theory predicts this transition to occur when  $\gamma_{gb} = 2\gamma_{sl}$ . Now consider the different curves of  $\gamma_{gb}$  versus misorientation shown in Fig. 8. For the two lowest values of  $u$ , this curve intersects the line corresponding to twice  $\gamma_{sl}$  for a misorientation of  $\theta \approx 2^\circ$ , much smaller than the transition angle obtained from the curves  $w(u)$  in Fig. 6. However, with increasing  $u$ , this intersection point moves toward larger angles, and for the highest value of  $u$  investigated, the intersection is at about  $9^\circ$ . Furthermore, it was shown above that when the disjoining potential exhibits a minimum, its value at this minimum is equal to  $\gamma_{gb} - 2\gamma_{sl}$  at the melting point. Since the transition to repulsive grain boundaries occurs when this minimum disappears, it is to be expected that the correct transition angle is obtained when the criterion  $\gamma_{gb} = 2\gamma_{sl}$  is used with the grain-boundary energy calculated exactly at the melting point.

In order to obtain more precise information on this question, it would be desirable to have accurate values for the grain-boundary energy at the melting point as a function of misorientation. However, as already mentioned, it is numerically very difficult to obtain values for the grain-boundary energy close to the melting point, especially for angles close to the repulsive-to-attractive transition, since the grand potential differences between the different states become extremely small. The best way to obtain reliable data close to the transition is to

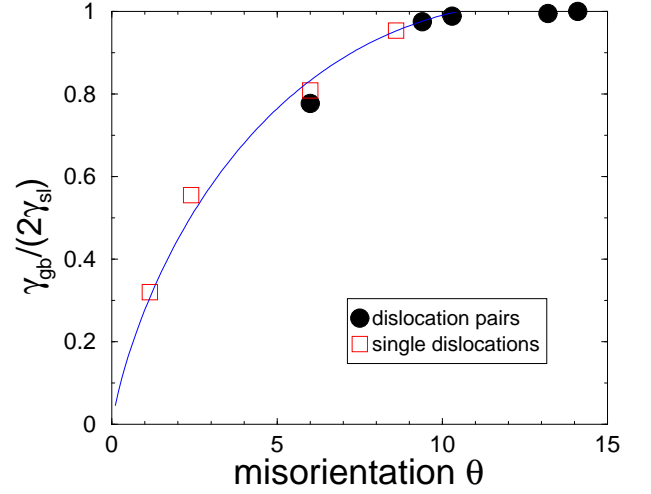


FIG. 11: Ratio of the grain-boundary energy and the melting point  $\gamma_g^m$  and twice the solid-liquid free energy as a function of misorientation for inclination  $\phi = 0^\circ$ . The line is a fit to the Read-Shockley law for the points with  $\theta < 10^\circ$ .

integrate Eq. (31) up to the melting point. The result is shown in Fig. 11; we estimate the error bars for these data to be on the order of the size of the symbols. For low-angle grain boundaries, the dependency of  $\gamma_{gb}$  on  $\theta$  can still be described by the Read-Shockley law. However, for higher angles, when the grain boundaries consist of dislocation pairs, the dependence of  $\gamma_{gb}$  on  $\theta$  is extremely weak: for  $\theta = 10.4^\circ$ , which is the first point that clearly deviates from the Read-Shockley law,  $\gamma_{gb}/(2\gamma_{sl}) \approx 0.99$ , so that the variation of  $\gamma_{gb}$  between this misorientation and the first repulsive grain boundary at  $14.1^\circ$  is only about 1%. Clearly, it is very difficult to describe precisely this regime. In addition, it is not clear whether it is generic, since the grain boundaries of inclination  $\phi = 30^\circ$  do not exhibit the structural transition to dislocation pairs.

A very interesting point is that the Read-Shockley law is still valid for low-angle grain boundaries, even at the melting point. This can be used to obtain a reasonable estimate for the critical angle as the solution of the equation

$$\frac{Ga}{4\pi\alpha(1-\sigma)}\theta_c [1 - \ln(2\pi\theta_c) + \ln(\alpha a/r_0)] = 2\gamma_{sl}. \quad (38)$$

However, it is crucial to take into account the variation of the grain-boundary energy with chemical potential (or temperature). Indeed, the values for the grain-boundary energy are usually determined in experiments or atomistic simulations for temperatures far below the melting point. As pointed out above, if these values are used to predict the critical angle, a completely wrong result is obtained. The variation of the grain-boundary energy with chemical potential (or temperature) arises from two distinct effects: the variation of the shear modulus and

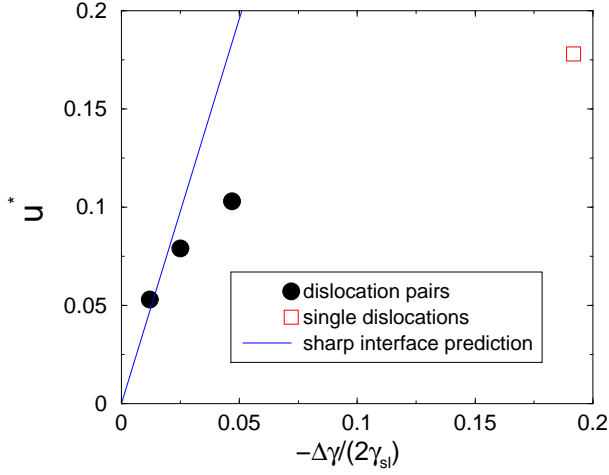


FIG. 12: Critical value  $u^*$  that corresponds to the limit of superheated states associated with the breaking of solid bridges. Symbols: simulation results, line: sharp-interface prediction according to Eq. (40).

the premelting around dislocations, which leads to an increase of the core radius in the Read-Shockley law as shown in Fig. 8. If the “low-temperature” values for both  $G$  and  $r_0$  are used in Eq. (38), we find  $\theta_c \approx 2^\circ$  (see Fig. 8), clearly too low. If only the variation of  $G$  is included (that is, Eq. (38) is used with the value of the shear modulus at the melting point, but with the low-temperature value  $r_0 = 3.5$  for the core radius), the prediction becomes  $\theta_c \approx 6^\circ$ . Finally, the improved estimate corresponding to Eq. (6) is obtained when the values at the melting point of both the shear modulus and the core radius are used, which yields the prediction  $\theta_c \approx 10^\circ$ . The curve of  $\gamma_{gb}^m$  that is obtained with these parameters is shown in Fig. 11. Clearly, the limited accuracy of this final estimate is due to the fact that the Read-Shockley law applies to grain-boundary states with individual dislocations. Thus, it does not take into account the complex structural changes in the boundary, which will tend to reduce the grain-boundary energy further from its value estimated from the Read-Shockley law. Therefore, the value of  $\theta_c$  obtained from this law is likely to be a lower bound estimate of the actual value.

Let us now come to the estimation of the critical value  $u_*$  that limits the range of “overheated” states. The transposition of the sharp-interface prediction, Eq. (4), to our variables is

$$\omega_l(u^*) - \omega_s(u^*) = -\frac{\Delta\gamma}{\delta}. \quad (39)$$

Expanding the grand potential around the melting point, and using the definition of  $u$ , Eq. (35), we find

$$u^* = - \left[ \frac{2\gamma_{sl}}{\frac{\partial \mu}{\partial \psi_s} \Big|_{\bar{\psi}_s^{\text{eq}}} (\bar{\psi}_s^{\text{eq}} - \bar{\psi}_l^{\text{eq}})^2 \delta} \right] \frac{\Delta\gamma}{2\gamma_{sl}}. \quad (40)$$

The ratio in brackets on the right-hand side can be calculated using the values from Table I and the values  $\delta \approx 5.8$  and  $2\gamma_{sl} \approx 0.00192$  extracted from our simulations (see Fig. 6). From the preceding discussion, it is clear that a reasonable estimate can only be obtained if  $\Delta\gamma$  is calculated with the grain-boundary energy at the melting point. In Fig. 12, we plot the values of  $u^*$  obtained from our simulations (that is, the values of  $u$  where the curves of  $w(u)$  terminate) versus  $-\Delta\gamma/(2\gamma_{sl})$ , using the values for  $\gamma_{gb}$  in Fig. 11, together with the theoretical prediction. It can be seen that this prediction gives reasonable values for the grain boundaries close to the transition that consist of dislocation pairs, even if the simulation data cannot be well described by a straight line. In contrast, the sharp-interface theory strongly overestimates the value of  $u^*$  for low-angle grain boundaries consisting of single dislocations.

The failure of the sharp-interface theory to predict the superheated range of grain boundaries is not surprising since the liquid phase domains consist of liquid pools instead of a thin liquid film of constant thickness as assumed in this theory. Recently, Berry *et al.*<sup>26</sup> developed a simple theory of grain-boundary wetting tailored to the liquid-pool geometry, which assumes that wetting occurs when pools coalesce, or, equivalently, when their radius  $r$  is equal to half of the distance  $d$  between dislocations. By calculating the shift of the melting point due to the dislocation elastic strain energy, they also obtained the scaling relation  $u^* \sim -(a/d)^2$ , where the dimensionless proportionality constant is related to the elastic constants. This scaling relation, together with the geometrical coalescence condition  $r = d/2 = a/(2\sin\theta)$ , yields the prediction  $u^* \sim -\sin^2\theta$ . As shown in Fig. 13, our results for the grain boundaries of the  $\phi = 30^\circ$  inclination that consist of unpaired liquid pools indeed show that  $u^*$  is reduced by an amount proportional to  $\sin^2\theta$ , consistent with this prediction. One important difference, however, is that the  $\theta = 0$  intercept of the curve  $u^*(\theta)$  is finite in our simulations, consistent with the existence of superheated metastable grain boundaries, while the theory of Berry *et al.*<sup>26</sup> predicts that liquid pools always coalesce below the melting point ( $u^*(0) = 0$ ). We expect  $u^*(\theta)$  to be generally positive in the limit of vanishing misorientation since a finite bulk thermodynamic driving force favoring the liquid phase is necessary to overcome the nucleation barrier imposed by the solid-liquid interfacial energy, which remains finite even in the presence of elastic strain energy around the dislocation cores.

It is interesting to note that the linear interpolation of the data in Fig. 13 predicts that  $u^*$  vanishes for  $\sin^2\theta \approx 0.06$ , which corresponds to a misorientation of  $14.6^\circ$ , in good agreement with our previous estimate for  $\theta_c$ . For misorientations above this value, no overheated states can exist, and there is hence no discontinuous transition between “dry” and “wet” grain-boundary states.

To further test this theoretical picture for the  $\phi = 30^\circ$  inclination, we have extracted the pool radius from the data for the film thickness using the simple geometrical

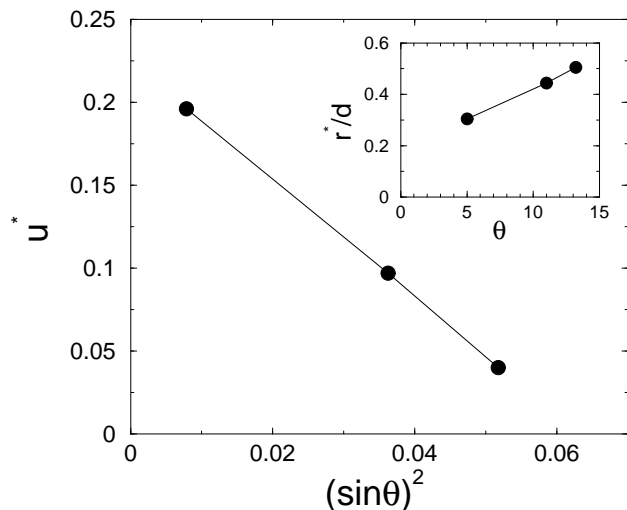


FIG. 13: Critical value  $u^*$  versus  $\sin^2 \theta$  for low-angle grain boundaries of inclination  $\phi = 30^\circ$ . Inset: Ratio of the liquid-pool radius  $r^*$  where the break-off occurs and the dislocation spacing  $d$  versus misorientation.

transformation

$$r = \sqrt{\frac{wL_x}{n_d\pi}}, \quad (41)$$

where  $n_d$  is the number of dislocations present in the system. Note that this pool radius differs from the dislocation core radius  $r_0$  extracted from the fits to the Read-Shockley law. As shown in the inset of Fig. 13, the pool radius at the break-off point,  $r^*$ , is not proportional to the dislocation spacing. Furthermore, the size of the liquid pools, as defined by Eq. (41) (which is of course equivalent to a Gibbs construction performed for a cylinder around a dislocation instead of a flat homogeneous liquid layer), is not uniquely determined by  $u$ , but also depends on the misorientation. This indicates that the above picture needs to be refined in order to better understand the condition for the coalescence of liquid pools above the melting point.

As a last point, it should be recalled that diffuse-interface theories of grain boundaries where the grain orientation is treated as a scalar order parameter have shown the possibility that two distinct grain-boundary states of markedly different widths can exist at the same temperature<sup>27,28</sup>. In contrast, aside from the dislocation-pairing hysteretic transition, we have found here the grain-boundary width to be uniquely determined at fixed chemical potential. However, we cannot rule out the existence of such two-state coexistence for crystal structures and grain-boundary orientations other than those investigated here, or in a narrow range of chemical potential very close to the melting point where numerical calculations with the PFC model become exceedingly difficult. Clearly, this question warrants further investigation.

## VI. CONCLUSIONS AND OUTLOOK

We have performed a detailed study of grain-boundary premelting using the phase-field crystal model. Our results demonstrate that there is a qualitative difference between high-angle “repulsive” and low-angle “attractive” grain boundaries. In the former, a continuous liquid film forms below the melting point, exhibiting a width that diverges when the melting point is approached from below. For low-angle grain boundaries, melting starts at individual dislocations. The grain boundary can be overheated up to a misorientation-dependent critical temperature at which the solid “bridges” between the liquid “pools” break and the system becomes liquid. Furthermore, we have found that a hysteretic structural transition from single dislocations to dislocation pairs can occur for intermediate values of the misorientation. The latter, however, is generally dependent on inclination since it is observed here for  $\phi = 0^\circ$  but not  $\phi = 30^\circ$ .

We have extracted numerically the dependence of the disjoining potential  $V(w)$  as a function of layer width  $w$ , and found that its shape is qualitatively different for high- and low-angle boundaries. For high angles,  $V(w)$  is purely repulsive for all  $w$  and reasonably well fitted by the exponential law of Eq. (1), assumed in sharp-interface theories<sup>1,8</sup>, at least for the largest misorientation investigated here. In contrast, for low-angle grain boundaries,  $V(w)$  is attractive for large  $w$ , but repulsive for small  $w$ , and exhibits a minimum that corresponds to the existence of a liquid layer of finite width at the melting point. Furthermore, this width diverges as the misorientation approaches from below a critical value  $\theta_c$  that distinguishes these two regimes. This divergence is smooth and reflects the progressive formation of a continuous premelted layer by merging of liquid-like pools and disappearance of solid bridges between them with increasing misorientation.

We have found that  $\theta_c$  is not well predicted by the exponential form assumed in Eq. (1) with a constant prefactor. This form does not describe the large reduction of the grain-boundary energy due to both the decrease of the shear modulus at high homologous temperature, and local melting around dislocations that is already present for low-angle boundaries. We have found that, in contrast, a Read-Shockley law for the grain-boundary energy used in conjunction with a value of the shear modulus at the melting point and an effective dislocation core radius, which describes phenomenologically dislocation-induced melting, yields a three to four times larger estimate of  $\theta_c$  that is in better agreement with the value obtained from PFC simulations. This estimate, however, is still too low due to the fact that dislocations are not isolated for  $\theta \approx \theta_c$  as assumed in the derivation of this law.

While this work has yielded a consistent picture of the thermodynamics of premelting in a microscopic model that can hopefully serve as a basis for developing more accurate mesoscopic models, it has also shown that many questions still need to be answered before a truly quan-

tative description can be obtained. First, and most importantly, how does the disjoining potential depend generally on crystal structure and grain-boundary orientation characterized by five parameters in the extension of this work to three dimensions? While developing a complete theoretical description of this potential seems difficult, there is reasonable hope that the interaction of crystal-melt interfaces due to the overlap of density-wave profiles for large separation ( $w \gg \delta$ ) could be understood within the framework of the Ginzburg-Landau theory<sup>33,34</sup>. The order parameters of this theory are the complex amplitudes of crystal density waves in the solid and one would expect the range of interaction of the disjoining potential to be related to the rate of spatial decay of these density waves in the liquid. The fact that this theory can be derived from the PFC model and related quantitatively to experiments and MD simulations for isolated crystal-melt interfaces<sup>34</sup> suggests that it should provide a fruitful theoretical framework in which to understand fundamental aspects of grain-boundary premelting. In particular, an asymptotic description of the disjoining potential for large  $w$  could in principle shed light on the physics of the critical wetting angle.

Let us finally comment on the further perspectives of our work. Here, we have only investigated the structural aspect of grain-boundary premelting. It would be interesting to study its consequences on macroscopic properties such as the resistance to shear. In principle, shear can be incorporated into the PFC model by modifying its equations of motion<sup>22</sup>. Since the experimental evidence for grain-boundary premelting in pure substances is controversial, whereas this phenomenon is well documented in alloys, it would also be interesting to extend our study to this case using recently developed PFC models for alloys<sup>24</sup>.

### Acknowledgments

This research was supported by a CNRS travel grant as well as by U.S. DOE through Grant No. DE-FG02-07ER46400 and the DOE Computational Materials Science Network program. We thank Robert Spatschek for many useful discussions and for a careful reading of the paper.

## APPENDIX A: IMPLEMENTATION OF THE PFC MODEL

### 1. Locally conserved dynamics

The standard locally conserved dynamics for the density field  $\psi$  is given by Eq. (15) as

$$\begin{aligned}\partial_t \psi &= (1 - \epsilon) \nabla^2 \psi + 2 \nabla^4 \psi + \nabla^6 \psi + \nabla^2 \psi^3 \\ &\equiv \hat{L} \psi + f,\end{aligned}$$

where the second equality defines the linear operator  $\hat{L} \equiv (1 - \epsilon) \nabla^2 + 2 \nabla^4 + \nabla^6$  and the nonlinear function  $f \equiv \nabla^2 \psi^3$ .

To avoid the numerically challenging gradient terms in real space, the equation of motion is solved in Fourier space. Multiplying both sides of the equation by  $\exp(ikx)$  and integrating over the entire volume leads to

$$\partial_t \tilde{\psi}_k = \hat{L}_k \tilde{\psi}_k + \tilde{f}_k, \quad (\text{A1})$$

where the Fourier modes of the density are  $\tilde{\psi}_k = \int \psi \exp(i\vec{k}\vec{x}) d\vec{x}$ ,  $\hat{L}_k = (\epsilon - 1)k^2 + 2k^4 - k^6$  is the linear operator in Fourier space, and  $\tilde{f}_k$  is the Fourier transform of the nonlinear function  $f$ .

Furthermore, an implicit integration scheme is used which allows us to use larger time steps. Instead of solving Eq. (A1) directly, it can be rewritten by using the ansatz  $\tilde{\psi}_k = u(t) \exp(\hat{L}_k t)$ . One then obtains

$$\begin{aligned}\partial_t \tilde{\psi}_k &= \hat{L}_k \exp(\hat{L}_k t) u(t) + (\partial_t u) \exp(\hat{L}_k t) \\ &= \hat{L}_k \exp(\hat{L}_k t) u(t) + \tilde{f}_k,\end{aligned}$$

so that  $\partial_t u(t) = \exp(-\hat{L}_k t) \tilde{f}_k$ . Integrating over time from  $t$  to  $t + \Delta t$  gives

$$u(t + \Delta t) - u(t) = \int_t^{t+\Delta t} dt' \exp(-\hat{L}_k t') \tilde{f}_k(t')$$

and with  $u(t) = \exp(-\hat{L}_k t) \tilde{\psi}_k(t)$  in terms of  $\tilde{\psi}_k$

$$\begin{aligned}\exp[-\hat{L}_k(t + \Delta t)] \tilde{\psi}_k(t + \Delta t) - \exp(-\hat{L}_k t) \tilde{\psi}_k(t) \\ = \int_t^{t+\Delta t} dt' \exp(-\hat{L}_k t') \tilde{f}_k(t') .\end{aligned}$$

Even if  $\tilde{f}_k$  is not known as a function of  $t$ , it can be expanded in a good approximation around  $t' = t$ , leading to

$$\begin{aligned}\tilde{\psi}_k(t + \Delta t) &= e^{\Delta t \hat{L}_k} \tilde{\psi}_k(t) \\ &+ e^{\hat{L}_k(t+\Delta t)} \int_t^{t+\Delta t} dt' e^{-\hat{L}_k t'} \\ &\times \left[ \tilde{f}_k(t) + \frac{\tilde{f}_k(t) - \tilde{f}_k(t - \Delta t)}{\Delta t} (t' - t) \right] \\ &= e^{\Delta t \hat{L}_k} \tilde{\psi}_k(t) + \frac{\tilde{f}_k(t)}{\hat{L}_k} (e^{\hat{L}_k \Delta t} - 1) \\ &+ \frac{\tilde{f}_k(t) - \tilde{f}_k(t - \Delta t)}{\Delta t \hat{L}_k^2} (e^{\hat{L}_k \Delta t} - 1 - \Delta t \hat{L}_k) .\end{aligned} \quad (\text{A2})$$

### 2. Non-local globally conserved dynamics

To accelerate the search for the equilibrium solution, a different non-local dynamical formulation can be used

where the dynamics depends globally on the density field, as opposed to locally in the standard conserved dynamics. The global conservation of the order parameter has then to be ensured by a Lagrange multiplier.

The conservation condition for  $\psi$  is given as

$$\int \psi(\vec{x}) d\vec{x} - L_x L_y \bar{\psi} = 0,$$

where  $\bar{\psi} = 1/(L_x L_y) \int \psi(\vec{x})$  is the average density. The free energy, including the constraint, can then be written as

$$\tilde{\mathcal{F}} = \mathcal{F} + \mu \left[ \int \psi(\vec{x}) d\vec{x} - L_x L_y \bar{\psi} \right].$$

where  $\mu$  is the Lagrange multiplier.

The equation of motion becomes

$$\begin{aligned} \partial_t \psi &= -\frac{\delta \mathcal{F}}{\delta \psi} + \mu \\ &= [(\epsilon - 1) - 2\nabla^2 - \nabla^4] \psi - \psi^3 + \mu \\ &\equiv \hat{L}\psi + f, \end{aligned}$$

where now  $\hat{L} \equiv (\epsilon - 1) - 2\nabla^2 - \nabla^4$  and  $f \equiv -\psi^3 + \mu$ . In Fourier space, the linear operator and the nonlinear function are given as  $\hat{L}_k = (\epsilon - 1) + 2k^2 - k^4$  and  $\tilde{f}_k = -\tilde{\psi}_k^3 + \tilde{\mu}_k$ , where  $\tilde{\psi}_k$  is the Fourier transform of  $\psi^3$  and  $\tilde{\mu}_k$  is that of  $\mu$ . Since  $\mu$  is a constant,  $\tilde{\mu}_k \propto \delta(k)\mu$ . With this  $\hat{L}_k$  and  $\tilde{\mu}_k$ , the implicit integration scheme as given in Eq. (A2) can be used.

The Lagrange multiplier  $\mu$  can be obtained from the condition

$$\begin{aligned} 0 = \partial_t \bar{\psi} &= \frac{1}{L_x L_y} \int \partial_t \psi(\vec{x}) d\vec{x} \\ &= \frac{1}{L_x L_y} \int \left[ -\frac{\delta \mathcal{F}}{\delta \psi} + \mu \right] d\vec{x}, \end{aligned}$$

or

$$\begin{aligned} \mu &= \frac{1}{L_x L_y} \int \frac{\delta \mathcal{F}}{\delta \psi} d\vec{x} \\ &= \frac{1}{L_x L_y} \int [(1 - \epsilon)\psi(\vec{x}) + \psi^3(\vec{x})] d\vec{x}, \end{aligned}$$

since the integral over the gradients is zero for a periodic system.

## APPENDIX B: BOUNDARY CONDITIONS

The two-dimensional hexagonal periodic solution given by Eq. (10) exhibits close-packed rows of density peaks along the  $x$  direction and can be described by two basis vectors  $\vec{a} = a(1, 0)$  and  $\vec{b} = a(1/2, \sqrt{3}/2)$ , where  $a = 2\pi/q = 4\pi/\sqrt{3}$  is the “lattice spacing” (the spacing between density peaks). When the entire structure is rotated by an angle  $\Theta$  ( $x \rightarrow x \cos \Theta + y \sin \Theta$  and

$y \rightarrow -x \sin \Theta + y \cos \Theta$ ), the rotated basis vectors are

$$\vec{a} = a \begin{pmatrix} \cos \Theta \\ -\sin \Theta \end{pmatrix} \quad \text{and} \quad (B1a)$$

$$\vec{b} = a \begin{pmatrix} \frac{1}{2} \cos \Theta + \frac{\sqrt{3}}{2} \sin \Theta \\ -\frac{1}{2} \sin \Theta + \frac{\sqrt{3}}{2} \cos \Theta \end{pmatrix}. \quad (B1b)$$

In order to exactly fit a periodic structure into the simulation box, a displacement of once the box size along the box axes must correspond to an integer number of steps along the two basis vectors, that is, we must have

$$n\vec{a} - m\vec{b} = \begin{pmatrix} L_x \\ 0 \end{pmatrix} \quad \text{and} \quad (B2a)$$

$$-i\vec{a} + j\vec{b} = \begin{pmatrix} 0 \\ L_y \end{pmatrix}, \quad (B2b)$$

where (without loss of generality)  $0 < \Theta < \pi/3$ , and  $n, m, i$  and  $j$  are integer numbers. The minus signs have been chosen by convention such that the conditions can be satisfied with positive integers.

From the components of the above vector equations that have a zero on the right hand side, we obtain two conditions for the angle,

$$\tan \Theta = \sqrt{3} \frac{m}{2n + m} \quad \text{and} \quad (B3a)$$

$$\tan \Theta = \frac{1}{\sqrt{3}} \frac{2i - j}{j}. \quad (B3b)$$

Only angles can be simulated for which four suitable integers can be found that satisfy both conditions. Note that with sufficiently large integers, any angle can be approximated to arbitrary precision. Once the four integers are determined, the dimensions of the simulation box are given by

$$L_x = a \left[ \left( n - \frac{m}{2} \right) \cos \Theta - m \frac{\sqrt{3}}{2} \sin \Theta \right], \quad (B4a)$$

$$L_y = a \left[ \left( \frac{j}{2} - i \right) \sin \Theta + j \frac{\sqrt{3}}{2} \cos \Theta \right]. \quad (B4b)$$

For the numerical treatment, the equations have to be discretized. In order to accommodate both conditions for the system size, in general slightly different grid spacings have to be used along the  $x$  and  $y$  directions since the ratio  $L_x/L_y$  may be irrational and cannot be well approximated by a single grid spacing. We always chose grid spacings  $\Delta x$  and  $\Delta y$  that are close to  $\pi/4$ , as in previous PFC studies<sup>19,20</sup>. We have checked by repeating selected runs with different choices for the discretization that grid effects are negligible for all the results presented here.

In the presence of grain boundaries, the density field is no longer periodic in the  $y$  direction, and Eq. (B4b)

for  $L_y$  does not apply. In this case, no simple condition for  $L_y$  can be given that ensures a strain-free bulk solid, since this would require a detailed knowledge of the grain-boundary structure. However, this condition is not as stringent as for single crystals since there is an additional degree of freedom: the dislocations present at the grain boundaries can move along the boundaries in response to bulk stress until a minimum of the energy is reached, which implies a relaxation of the bulk stress. Even if there is only a finite number of dislocation positions that correspond to a local energy minimum (this number scales as  $d/a$ , where  $d$  is the distance between dislocations), as long as  $L_y$  is chosen to be much larger than  $L_x$ , the residual bulk stresses should be very weak. Indeed, we have varied  $L_y$  by small amounts for several sets of parameters, and never found significant variations in the free-energy density.

It should be noted that the condition on  $L_x$ , Eq. (B4a) still applies. For low-angle grain boundaries, the numbers  $m$  and  $n$  can easily be related to explicit dislocation models. For instance, consider the  $\phi = 0^\circ$  inclination:

the number  $m$  corresponds to the number of close-packed planes that originate at the grain boundary for each of the two tilted grains; the total number of edge dislocation is therefore equal to  $2m$ . In turn,  $n$  indicates the number of steps that have to be taken along a close-packed row before a site that is geometrically equivalent to the starting site can be reached by  $m$  steps along the basis vector  $\vec{b}$ . While the average spacing  $d$  between dislocations is therefore always equal to  $L_x/(2m)$ , the minimum-energy configuration does not always correspond to equal spacings between dislocations. For instance, for  $m = 1$ ,  $n$  even yields two dislocations that are evenly spaced, whereas  $n$  odd corresponds to a grain boundary where a slightly larger and smaller spacing alternate along the interface. Such configurations are well known<sup>36</sup> and constitute a local energy minimum. We did not notice any considerable difference between the behaviors of these two types of grain boundaries. This is to be expected since, due to the condition on  $L_x$  in Eq. (B4b), the system is still globally strain-free far from the grain boundary.

- 
- <sup>1</sup> M. Rappaz, A. Jacot, and W. J. Boettinger, *Metall. Mater. Trans. A* **34**, 467 (2003).
  - <sup>2</sup> N. Wang, S. Mokadem, M. Rappaz, and W. Kurz, *Acta Mater.* **52** 3173 (2004).
  - <sup>3</sup> M. E. Glicksman and C. L. Vold, *Surf. Sci.*, **31**, 50 (1972).
  - <sup>4</sup> T. E. Hsieh and R. W. Balluffi, *Acta Metall.*, **37**, 1637 (1989).
  - <sup>5</sup> S. Divinski, M. Lohmann, C. Herzig, B. Straumal, B. Baretzky, and W. Gust, *Phys. Rev. B* **71**, 104104 (2005).
  - <sup>6</sup> A. M. Alsayed, M. F. Islam, J. Zhang, P. J. Collings, A. G. Yodh, *Science*, **309**, 1207 (2005).
  - <sup>7</sup> J. Q. Broughton and G. H. Gilmer, *Phys. Rev. Lett.* **56**, 2692 (1986).
  - <sup>8</sup> J. Q. Broughton and G. H. Gilmer, *J. Phys. Chem.* **91**, 6347 (1987).
  - <sup>9</sup> J. Q. Broughton and G. H. Gilmer, *Modell. Simul. Mater. Sci. Eng.* **6**, 87 (1998).
  - <sup>10</sup> T. Nguyen, P. S. Ho, T. Kwok, C. Nitta, and S. Yip, *Phys. Rev. B* **46**, 6050 (1992).
  - <sup>11</sup> S. Zhao, D. Cheng, S. Wang and H. Ye, *J. Phys. Soc. Jpn.* **70**, 733 (2001).
  - <sup>12</sup> W. Fan and X.-G. Gong, *Phys. Rev. B* **72** 064121 (2005).
  - <sup>13</sup> S. von Althaus, K. Kaski, and A. P. Sutton, *Phys. Rev. B* **76**, 245317 (2007).
  - <sup>14</sup> R. Kikuchi and J. W. Cahn, *Phys. Rev. B* **21**, 1893 (1980).
  - <sup>15</sup> G. Besold and O. G. Mouritsen, *Phys. Rev. B* **50**, 6573 (1994).
  - <sup>16</sup> In the  $(N, p, T)$  ensemble, the volume is not constant; therefore, strictly speaking, Gibbs free energies per particle should be used rather than per unit volume. However, it can be shown that the two approaches are equivalent here. For simplicity, we neglect the interfacial energies and write the Gibbs free energy as  $G = N_s g_s + N_l g_l$ , where  $N_s$  and  $N_l$  are the numbers of particles in the solid and the liquid (with  $N_l + N_s = N$  fixed), and  $g_s$  and  $g_l$  are the free energies per particle in the solid and the liquid. Subtracting the value for a homogeneous solid,  $N g_s$ , and dividing by the total surface area  $A$  of the liquid film, we obtain  $G_{\text{exc}} = (N_l/A)(g_l - g_s)$  which can be rewritten as  $G_{\text{exc}} = (N_l V_l/A)[(g_l - g_s)/V_l]$  where  $V_l$  is the volume per particle in the liquid. The expression used in Eq. (1) is obtained by identifying  $w = N_l V_l/A$  and  $\Delta G = (g_l - g_s)/V_l$ .
  - <sup>17</sup> C. S. Smith, *Trans. Am. Soc. Met.* **45**, 533 (1953).
  - <sup>18</sup> P. G. de Gennes, *Rev. Mod. Phys.* **57**, 827 (1985).
  - <sup>19</sup> K. R. Elder, M. Katakowski, M. Haataja and M. Grant, *Phys. Rev. Lett.* **88**, 245701 (2002).
  - <sup>20</sup> K. R. Elder and M. Grant, *Phys. Rev. E* **70**, 051605 (2004).
  - <sup>21</sup> N. Goldenfeld, B. P. Athreya, and J. A. Dantzig, *Phys. Rev. E* **72**, 020601(R) (2005).
  - <sup>22</sup> P. M. Stefanovic, M. Haataja, and N. Provatas, *Phys. Rev. Lett.* **96**, 225504 (2006).
  - <sup>23</sup> J. Berry, M. Grant, and K. R. Elder, *Phys. Rev. E* **73**, 031609 (2006).
  - <sup>24</sup> K. R. Elder, N. Provatas, J. Berry, P. Stefanovic, and M. Grant, *Phys. Rev. B* **75**, 064107 (2007).
  - <sup>25</sup> T. V. Ramakrishnan and M. Yussouff, *Phys. Rev. B* **19**, 2775 (1979).
  - <sup>26</sup> J. Berry, K. R. Elder, and M. Grant, *Phys. Rev. B* **77**, 224114 (2008).
  - <sup>27</sup> A. E. Lobkovsky and J. A. Warren, *Physica D* **164**, 202 (2002).
  - <sup>28</sup> M. Tang, W. C. Carter, and R. M. Cannon, *Phys. Rev. B* **73**, 024102 (2006).
  - <sup>29</sup> R. Lipowsky, *Phys. Rev. Lett.* **57**, 2876 (1986).
  - <sup>30</sup> D. R. Clarke, *J. Am. Ceram. Soc.* **70**, 15 (1987).
  - <sup>31</sup> K. van Benthem, G. Tan, L. K. DeNoyer, R. H. French, and M. Rühle, *Phys. Rev. Lett.* **93**, 227201 (2004).
  - <sup>32</sup> J. W. Cahn, *J. Chem. Phys.* **66**, 3667 (1977).
  - <sup>33</sup> K.-A. Wu, A. Karma, J. J. Hoyt and M. Asta, *Phys. Rev. B* **73**, 094101 (2006).
  - <sup>34</sup> K.-A. Wu and A. Karma, *Phys. Rev. B* **76**, 184107 (2007).
  - <sup>35</sup> S. M. Foiles, *Phys. Rev. B* **49**, 14930 (1994).
  - <sup>36</sup> W. T. Read and W. Shockley, *Phys. Rev.* **78**, 275 (1950).
  - <sup>37</sup> J. Swift and P. C. Hohenberg, *Phys. Rev. A* **15**, 319 (1977).

<sup>38</sup> S. Chandrasekhar, Rev. Mod. Phys. **21**, 383 (1949).

<sup>39</sup> J. W. Cahn, p. 379 in *The Selected Works of John W. Cahn*, edited by W. C. Carter and W. C. Johnson, The Minerals, Metals, and Materials Society, Warrendale, PA (1998).

<sup>40</sup> The analogous quantity in the  $(N, p, T)$  ensemble for fixed pressure and varying temperature is  $u = (T - T_m)/(L/c_p)$ , where  $L$  is the latent heat of fusion and  $c_p$  the specific heat at constant pressure.

<sup>41</sup> We have  $G = Y/[2(1 + \sigma)]$ , where  $G$ ,  $Y$ , and  $\sigma$  are

the shear modulus, bulk modulus, and Poisson's ratio in three dimensions, respectively. In two dimensions, we have  $\sigma_2 = \sigma/(1 - \sigma)$  and  $Y_2 = Y/(1 - \sigma^2)$ . Inserting these relations in Eq. (36) transforms the prefactor into  $aY_2/(8\pi)$ , which is identical to the result of Ref.<sup>20</sup>, taking into account that the modulus of the Burgers vector of a standard edge dislocation in the two-dimensional hexagonal structure is equal to the lattice spacing.